A mechanistic modelling framework for swirling gas-liquid vertical pipe flow

INVESTIGATING THE BUBBLY TO COLUMNAR FLOW TRANSITION

MSC THESIS

Bart van der Zalm

A mechanistic modelling framework for swirling gas-liquid vertical pipe flow

INVESTIGATING THE BUBBLY TO COLUMNAR FLOW TRANSITION

MSC THESIS

to be defended on Wednesday, September 21, 2022 at 14:00

Bart van der Zalm
1303694

PROGRAMME

Applied Physics
Track Physics for Fluid Engineering

SUPERVISION

Dr. Luis Portela
Department of Chemical Engineering, Transport Phenomena Group

Matheus M. Garcia

THESIS COMMITTEE

Dr. Luis Portela
Prof. Dr. Ir. Ruud Henkes
Dr. Bijoy Bera

to Wing

for your loving support (and patience)

Abstract

The use of swirling motion for separating fluid-fluid mixtures based on their respective densities is a modern concept that allows for fast separation with only limited equipment size. For industrial exploitation it is desirable that this process can be controlled in order to optimize separation efficiency. This requires predictive models that produce fast yet accurate estimates on the complex, three-dimensional dynamics of swirling flows. In this thesis, a mechanistic modelling framework is developed for swirling gas-liquid pipe flow which, by considering only the key physical mechanisms, would allow for such predictions with relatively limited means. It is based on the two-fluid model and quasi-1D, disperse flow reasoning. As a benchmark case, this model is used to investigate the onset of fully separated, columnar flow patterns that are characteristic to swirling multiphase flow, for low gas input flows.

To first order, the swirling motion affects the radial distribution of phases through its local magnitude, and the axial pressure gradient through its rate of decay. It is concluded that both effects are required for accurate estimation of the relevant parameters for control. Empirical observations using an inline swirl separator indicate that the modelling framework correctly accounts for a non-homogeneous distribution of phases. Its prediction of the occurrence of columnar flow even for low mixture velocities at low gas flow rates was verified experimentally. The framework is in qualitative agreement with literature data on the axial velocity profile if an exponential swirl decay model is used as the only streamwise variation.

A qualitative transition criterion for the onset of columnar flow is proposed, using an analogy to the bubbly to slug transition in regular gas-liquid flow. Both transitions appear to be characterized by a two-stage process of clustering and coalescence of the gas phase — the difference in swirling flow is that these effects are forced to occur in a limited region of the pipe only.

Acknowledgements

I would like to thank Dr. Luis Portela for his guidance. Equal parts thorough and master of the hand-waving argument, his support has made it seem as if the complexity of multiphase flows is something you can just see through if you look closely.

I am also grateful to Matheus Garcia for sharing his insights on my research, and to the group technicians that aided in implementing the experiments (Evert, Stefan, Christiaan).

Contents

List of Figures

List of Tables

List of Symbols

Roman symbols

A	pipe area	m^2
B	scaling parameter of Gaussian vortex profile	m/s
C_{D}	drag coefficient	[–]
C_{L}	lift coefficient	[–]
d	particle diameter	m
D	pipe diameter	m
$\mathbb{D}_t$	turbulent dispersion coefficient	m^2/s
$\mathcal{F}_{\mathrm{N}i}$	interfacial momentum transfer of phase N	kg $\mathrm{m/s}^2$
g	gravitational acceleration	$\mathrm{m/s}^2$
j_{N}	superficial velocity of phase N	m/s
k	Von Kármán constant	[–]
L	integral length scale (mixing length)	m
p	local pressure	Pa
P	mean pressure	Pa
p'	pressure fluctuation	Pa
Q_{N}	volumetric flow rate of phase N	m^3/s
r	radial coordinate	m
R	pipe radius	m
R_c	core radius of Gaussian vortex profile	m
$u_{\mathrm{N}i}$	instantaneous/local velocity of phase N	m/s
U_i	continuous phase mean velocity	m/s
u'_i	continuous phase velocity fluctuation	m/s
u_*	friction velocity	m/s
U_0	slip velocity	m/s
V_i	disperse phase mean velocity	m/s
v'_i	disperse phase velocity fluctuation	m/s
y	wall normal coordinate	m
z	axial coordinate	m

Greek symbols

α_{N}	volumetric fraction of phase N	[–]
θ	tangential coordinate	rad
μ_{N}	dynamic viscosity of phase N	kg/m s
ν_{N}	kinematic viscosity of phase N	$\mathrm{m^2/s}$
ν_t	eddy viscosity	$\mathrm{m^2/s}$
ξ	swirl decay scaling parameter	[–]
ρ_{N}	density of phase N	$\mathrm{kg/m^3}$
σ	surface tension	$\mathrm{kg/s^2}$
$\tau_{\mathrm{N}ij}$	deviatoric stress tensor of phase N	kg/m s
Ω	swirl intensity	[–]

Other symbols

$\widetilde{x}$	area averaged/mixture quantity
$\overline{x}$	ensemble averaged quantity
$\langle x \rangle$	average at the position of the particle

Chapter 1

Introduction

1.1 Context

Separation of fluids by their relative density is a recurring objective in industrial settings. A particularly efficient approach to this problem is to incur a swirling motion in the fluid mixture to be separated. Similar to a centrifuge, the swirling motion effectively forces the denser fluid outward, allowing the lighter fluid to accumulate near the center of the resulting vortex, which yields a distinct separation in the plane of rotation.

A traditional approach to density-induced separation is the use of settling tanks, in which fluid mixtures are separated by gravitational forces over long time spans and with little flow. These tanks therefore require large dimensions in order to be of practical use. In comparison, the centripetal forces responsible for separation by swirling motion can be orders of magnitude stronger than their gravitational counterpart even for limited rotation rates. This means separation can be achieved faster and with reduced equipment size.

These benefits have led to the development of industrial hydrocyclones for fluid-fluid separation from the 1980s onwards [29]. Figure 1.1 illustrates the two common geometries, which are categorized by their inlet flow direction. A *tangential* cyclone creates its swirling motion by forcing a fluid mixture tangentially into a conical vessel. The denser fluid spirals down along the vessel wall to a bottom outlet while the lighter fluid is collected at the top. The geometry of the vessel and the inlet flow rate determine the efficiency of separation.

In an *axial* cyclone, a fluid mixture is brought into swirling motion by forcing it along a rigid body equipped with helical vanes, which is installed inside the flow conduit in the streamwise direction. The separated fluids are collected in concentric outlets situated further downstream. The angle of the vanes and the inlet flow rate determine the efficiency of separation. A particular advantage of axial cyclones is that there is only a relatively low pressure drop over the separation section.

Both hydrocyclone geometries are used heavily in industrial settings, as they are simple to operate and do not include any moving or electrical parts that are prone to failure. Examples of use include the separation of oil from water in the petrochemical industry, and the separation of liquid water from steam prior to entry into turbine generators in the nuclear power cycle [14, 20, 29].

Near real-time control strategies for swirl separation

In practical operation of hydrocyclones, the input fluid mixture generally has a variable composition in time. This affects the separation efficiency if the outlet conditions are fixed. In gas-liquid separation for example, a static outlet will collect additional liquid in the gas output stream whenever the instantaneous gas fraction in the mixture is low. At high gas fractions, the liquid output stream will feature excess gas not taken up by the outlet.

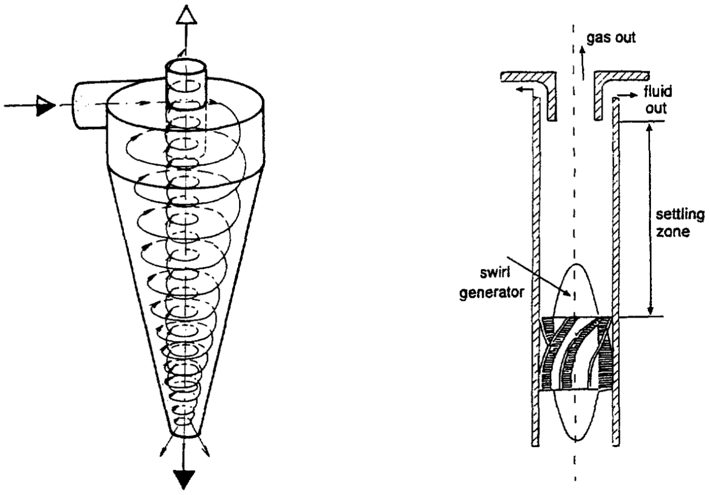

Figure 1.1: Hydrocyclone geometries — tangential (left) and axial (right).
reprint from [29]

Additionally, the complex dynamics of the swirling motion may oppose efficient separation at certain operating conditions, e.g. through hydrodynamic instabilities.

These effects can be counteracted by appropriate control strategies, that optimize for the quality of the output streams. However, the reduced timescales for swirl separation processes imply that their control needs to be very fast. This puts strong requirements on all sensing, data processing and actuation steps involved. As part of the TOMOCON European reseach programme, current research at TU Delft's Transport Phenomena group is aimed at near real-time control for swirl separation using tomographic sensors.[1] This research employs an axial cyclone in a vertical pipe to separate air-water mixtures of varying composition. Several combinations of feedback (output sensing) and feed-forward (input sensing) mechanisms are studied in order to develop control strategies deemed suitable for the process industry [20].

A particular challenge in this research is to develop simple predictive models that provide fast yet accurate control instructions. In general, computational fluid dynamics solvers are not well suited for this, as their runtime quickly outlasts the time available for control. A mechanistic modelling approach, which reduces the complexity of the swirl separation process by only considering its dominant physical mechanisms, appears more appropriate. This allows for sacrificing detail for speed, while retaining sufficient accuracy. However, a fundamental understanding of the dynamics of swirling flows is required for a proper judgment on retaining/discarding certain mechanisms. This thesis is aimed at increasing such understanding, in analogy to earlier work on gas-liquid flows without swirl.

1.2 Modelling of swirling gas-liquid flow

The dynamics of a mixture flow (or *multiphase* flow, as opposed to single-phase flow) are to a large extent governed by the way in which its constituents are distributed. Possible distributions are commonly categorized into distinct 'flow patterns', which can look wildly dissimilar even though all stem from the same governing equations. The occurrence of a particular flow pattern strongly influences pressure drop, heat and mass transfer rates, residence time and (back-)mixing [2]. When considering a control strategy for a multiphase process, these are exactly the parameters one is trying to enforce. It is therefore essential

---

[1] The website tomocon.eu/fluid-separation/ has additional information on this research.

to deduce the prevailing flow pattern a priori, by observation or through predictions based on the input flow conditions.

For gas-liquid flow without swirl, a series of mechanistic models have been developed in the 1970s and 80s that predict the prevailing flow pattern for given input conditions on the basis of simple criteria [2–5]. With considerable skill, their authors interpreted experimental observations to deduce the dominant mechanisms responsible for a transition from one flow pattern to the other. Their criteria quantify these transitions based on physical reasoning. Therefore, they are also applicable outside the scope of the experiments that were used to define them. This approach has proved to be very successful, and many of these models are still in widespread use throughout industry today.

In swirling gas-liquid flow, additional flow patterns can be observed that do not occur in regular mixture flow. As a result of phase separation, helical columns of gas form at the center of the swirling motion, with a (thick) liquid layer revolving around it. Depending on the input flow conditions and the intensity of swirl, these columnar flows can either be steady or display oscillatory behaviour, with sudden bursts along their trajectory or full breakup of the pattern after a certain length. These flow patterns have recently been mapped as a function of input conditions by different authors for various flow geometries, including the TOMOCON setup [6, 7, 34].

There is now considerable interest in a quantifiable characterization of these swirling flow patterns, in analogy to the earlier models developed for gas-liquid flow without swirl. A concrete modelling framework for swirling flow has not been established in the literature as of yet. Considerable difficulty to do so arises from the complex, three-dimensional nature of swirling flows: this only allows for limited idealizations to the flow without sacrificing essential physics involved. This thesis investigates the physical mechanisms involved in swirling gas-liquid flow, how these interplay and in what way they affect the flow patterns. From this understanding, it aims to construct a mechanistic modelling framework that can qualitatively explain the observed behaviour. As a benchmark case, this will be used to investigate the onset of stable columnar flow for low gas input flows. This pattern is the most elementary of the additional configurations found in swirling flow. The relation between the model output and the observations available should prove insightful for formulating (adjusted or new) transition criteria for swirling gas-liquid vertical pipe flow.

1.3 Thesis outline

This thesis is structured in three distinct parts — analysis, modelling, and experiments. The analysis part provides a background to gas-liquid flow patterns with and without swirl, and mechanistic modelling. The modelling part revolves around simplifying assumptions to the governing equations in order to obtain a simple model for swirling gas-liquid flow, on the basis of physical reasoning. This model is tested under various input conditions, in order to allow for experimental verification of its results. The experimental data obtained is discussed in the last part, in relation to the model output and its assumptions.

PART 1

Analysis

Chapter 2

Observations

This chapter serves as a background to the context of this thesis. It contains a visual guide to the different configurations of phases that are observed in gas-liquid vertical pipe flow, and details how these are categorized into flow patterns. Regular gas-liquid flow (without swirl) is discussed first, for the purpose of historical understanding and as a benchmark case: it is interesting to consider how the addition of swirling motion affects these patterns when other input conditions are kept equal. Section 2.3 illustrates the use of flow maps to deduce the prevailing flow pattern for certain input flow rates of gas and liquid.

For flow without swirl, there is relative consensus that the patterns treated in section 2.1 correctly cover the full spectrum of phase configurations that occur in practice. In swirling flow, the patterns discussed appear consistently throughout the literature, but there is no general agreement as to whether these represent all possible phase configurations. The list in section 2.2 should therefore be considered non-exhaustive.

2.1 Flow patterns in regular gas-liquid flow

Figure 2.1 illustrates the four basic flow patterns commonly observed in gas-liquid vertical pipe flow. In cyclone separators such as the TOMOCON setup, the input flow (prior to the addition of swirling motion) can consist of any of these four patterns. They are categorized from left to right by increasing gas fraction. In the limit situations of low and high gas content, a continuous carrier phase (liquid/gas) emerges, through or by which the other constituent is transported upward. This distinction is less clear for inbetween gas flow rates, where the associated pattern dynamics are more complex. The pattern descriptions below draw upon the work of Brennen, Taitel and others [23, 3].

Bubbly flow

At low gas flow rates, a configuration of discrete bubbles forms in a continuous liquid phase. These bubbles have an approximately uniform distribution over the pipe cross section. Their size and shape are governed by the characteristics of the liquid flow. If the gas fraction is slightly increased, a non-homogeneous bubbly flow results throughout which incidental, larger bubbles are present. The bubbly flow pattern classifies as a *disperse* flow. It is the starting point of the modelling framework developed in chapter 4.

Slug flow

Large, bullet-shaped gas bubbles that nearly span the entire cross section alternate periodically with regions of smaller gas bubbles dispersed in a continuous liquid 'slug'. A thin liquid film flows downward around the bigger bubbles into the slug. Bubble and slug dimensions are in equilibrium, and the total flow has a uniform upward direction.

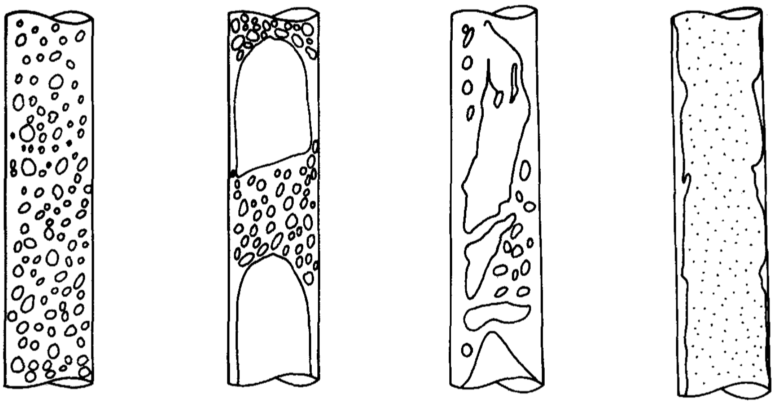

(a) bubbly (b) slug (c) churn (d) annular

Figure 2.1: Flow patterns occurring in regular gas-liquid flow, without swirl. *reprint from* [3]

Churn flow

Churn flow is characterized by disorderly, up- and downward motion of liquid and gas in local flow regions. Its composition resembles slug flow, but instead of stable bullet-shaped bubbles it features big chunks of gas of distorted shape, around which broken liquid slug falls. Whenever a liquid bridge across the pipe forms, it can be lifted by the gas until breakup re-occurs. These processes continuously alternate, and the unstable flow that results is difficult to quantify. This patterns is also referred to as ‘froth flow’.

Annular flow

In annular flow a broad, high velocity gas core is surrounded by a thin liquid film that flows along the perimeter. This core can also contain disperse liquid droplets, that are entrained from the rough interface of the film. The gas phase transports the liquid upward by drag forces, which are substantial due to the high relative velocity between the phases. The annular flow pattern classifies as a *separated* flow.

2.2 Flow patterns in swirling gas-liquid flow

The addition of swirl to a gas-liquid flow introduces an additional force mechanism to be reckoned with. Centripetal forces associated with the swirling motion act to separate the constituent phases by their respective density — in gas-liquid flow, this implies the gas phase is forced inward, and the liquid phase outward. This results in a non-homogeneous distribution of phases over the cross section, which affects the possible configurations of gas and liquid the mixture flow can settle in. Also, other configurations can occur than those described in section 2.1. As a consequence, a categorization of possible flow patterns depends both on the gas fraction and on the rate of swirl. In hydrocyclones, the latter is often related to the liquid flow rate, which is the predominant source of input momentum at limited gas flow rates.

An additional complication in defining suitable flow patterns for swirling flow is that these can only be sustained over limited lengths, due to the streamwise decay of the swirling motion. In contrast to their regular counterparts, swirling flow patterns are therefore in constant evolution. A coarse characterization into distinct patterns is formulated here, based on a review of recent literature. The pattern descriptions below draw upon observations on different hydrocyclone geometries, including the TOMOCON setup [6, 7, 34].

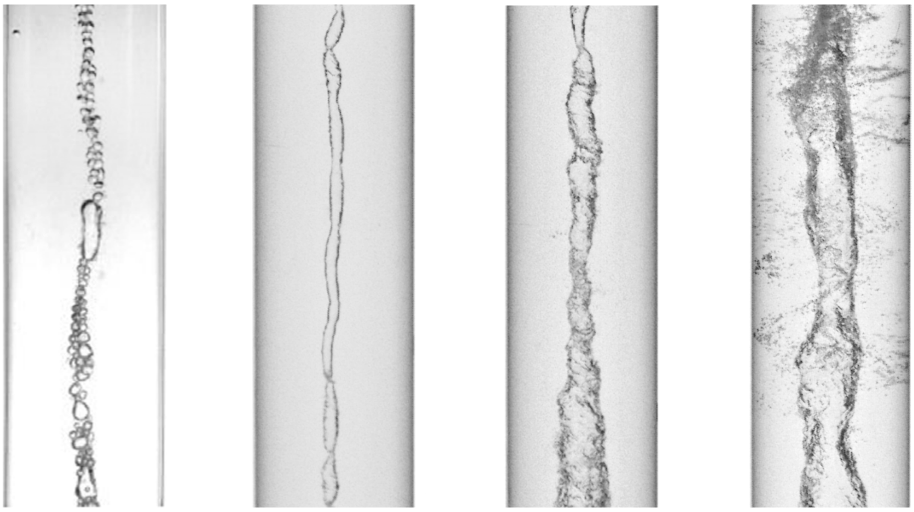

(a) clustered bubbly (b) stable columnar (c) pulsating columnar (d) intermittent columnar

Figure 2.2: Flow patterns occurring in swirling gas-liquid flow.
reprints from [7, 34]

Swirling ‘regular’ patterns

In cases where the swirling motion is not strong enough to significantly alter the phase configurations, the regular patterns from section 2.1 are recovered, with an additional helical component to their upward motion. This is most clearly observed for the bubbly and annular patterns, and less so for slug and churn due to their more chaotic nature.

Clustered bubbly flow

At low gas flow rates with swirl, several authors have observed a clustering of discrete bubbles near the centerline, and the formation of helical structures. Even though the local gas concentration is high, no coalescence occurs. In relation to the regular flow patterns, this has all the characteristics of bubbly flow, but with a non-homogeneous gas distribution due to the swirling motion. This pattern is also referred to as ‘chain flow’.

Stable columnar flow

A columnar flow is characterized by coalescence of the gas phase into a vertical (or slightly helical) stream, which is fully separated from the liquid phase surrounding it. This pattern is highly stable if the mixture composition prior to the application of swirl is homogeneous. It is therefore associated with regular bubbly flow. Visually however, it resembles annular flow, although its core is limited in diameter at low gas flow rates and the liquid forces are assumed to dominate the dynamics.

Pulsating columnar flow

An inhomogeneous mixture flow (e.g. slug or churn) to which swirl is applied results in a columnar flow that displays oscillatory behaviour as a result of variations in gas content. The gas core diameter widens and contracts. If the centripetal forces are strong enough to contain these sudden changes, the columnar pattern can be sustained, but shows pulsations along its length. This pattern is sometimes taken together with intermittent columnar flow due to their shared periodicity, even though the pulsating column remains continuous.

Intermittent columnar flow

Local breakup of a columnar pattern occurs when the swirl intensity is insufficient to contain large changes in gas content. This produces a burst of small disperse bubbles that spiral outward from the point of breakup, but soon after regroup in a columnar flow because the centripetal forces remain significant. This pattern is also referred to as ‘bursting columnar’.

2.3 Flow pattern mapping

From the 1950s onwards, much effort has been put in mapping the prevailing pattern of two-phase flows for given input conditions. These are two-dimensional plots in which the coordinate axes generally relate to the flow rates or the input momentum of each phase. From such maps, the boundaries between adjacent patterns can be roughly estimated. Such information is valuable for industrial settings in which flow cannot be readily observed, because it is indicative of pressure drop, heat and mass transfer rates, residence time, etc. However, the prevailing flow pattern also depends on various other parameters, such as the phase properties and the geometry used. Predictions based on flow maps are therefore only accurate if there is close similarity between flows. This is further addressed in chapter 3.

Pattern classification generally occurs on a visual basis. Because it is difficult to clearly distinguish between relatively unstable patterns, human error can be significant. As such, flow maps by different authors are not always in agreement. Figure 2.3 shows an example of a flow map constructed for swirling air-water flow in a tangential cyclone [6].

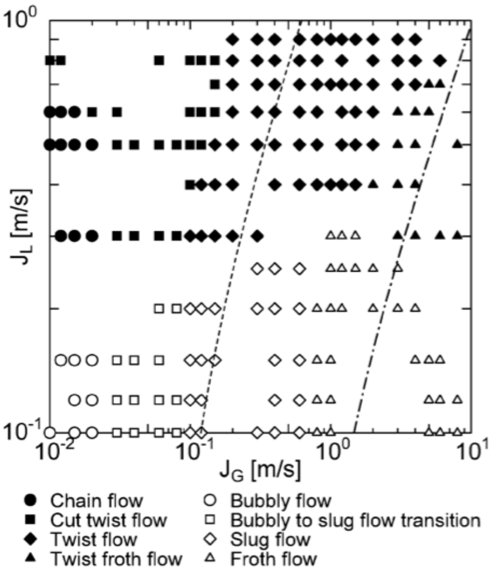

Figure 2.3: A flow map for swirling air-water flow in a tangential cyclone.
Regular patterns are depicted with open markers, columnar flow patterns with filled markers.
It follows that a columnar flow does not form below a certain threshold in the superficial liquid velocity j_L.
reprint from [6]

Chapter 3

Mechanistic modelling

This chapter provides a background on the mechanistic modelling approach and discusses its relevance for use in the context of this thesis.

3.1 Origins

A natural corollary of the many possible configurations in which gas-liquid flows can be distributed under certain flow conditions, is that resolving the two-phase problem in full from the governing equations is complex, even by today's computational standards. This has led to significant research in the 20th century into identifying assumptions that simplify the two-phase problem to make it analytically tractable.

In mechanistic modelling, simplified models are constructed on the basis of physical reasoning and empirical observation, with the aim to only resolve those aspects of the problem that are needed to produce qualitatively correct results. Less significant effects are left unconsidered or are accounted for by correction parameters. If the assumptions made reflect a correct understanding of the key phenomena, it is possible to obtain accurate estimates of complex problems with only limited means. The applicability of these simple models depends on the range of validity of the assumptions.

Mechanistic models have great value for use in industrial settings, where resolving the flow in full detail is either unnecessary or impossible (e.g. because of time or budget constraints[1]) and simple correlations suffice. A particular benefit is their ability to generalize to flows other than those used to establish the model, because the effects of different geometries and fluid parameters are correctly accounted for from physical understanding. This is where flow maps, as described in chapter 1, have only limited applicability: if the flow does not closely resemble both composition and operating conditions of the map, any prediction based on it is not likely to be reliable.

3.2 Use in demarcation of flow patterns

In most gas-liquid flows, a correct approach to modelling a problem depends strongly on the flow pattern. Many simplifying assumptions are specific to a certain configuration of the phases, e.g. disperse bubbles in a continuous liquid, and do not hold across different patterns. To deduce the prevailing flow pattern for certain input conditions is therefore an important first step in the solution of a multiphase flow problem.

The occurrence of a particular flow pattern depends on which physical mechanisms are dominant in a given flow region. Flow pattern boundaries are therefore commonly quantified with criteria based on non-dimensional numbers, that indicate the relative importance of

---

[1] As noted in the introduction, satisfying time constraints is a key objective in the TOMOCON research.

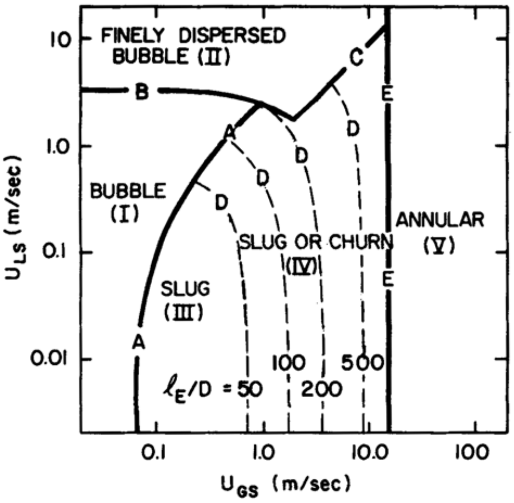

Figure 3.1: Transition curves between flow patterns for an air-water flow without swirl, based on mechanistic modelling. Curves A, B, E are elaborated on in section 3.3.
reprint from [3]

opposing forces. These numbers are calculated using the characteristic scales of the problem. Single-phase flow is a simple example, in which a Reynolds number threshold (Re $\gtrsim 2,000$ for pipe flow) is the criterion for transition from laminar to turbulent flow. The condition of turbulent flow subsequently allows for neglecting the effects of viscosity when computing estimates for the bulk of the flow.

In comparison, multiphase flows feature a much wider range of force mechanisms and complicated interdependencies between phases. A proper distinction between flow patterns for multiphase flows is therefore likely to depend on multiple criteria. It is important to note that transition boundaries are not clear-cut and the flow is highly sensitive to instabilities near these regions. Moreover, there can be considerable disagreement between authors on the exact mechanisms responsible for each transition. This is why in practice, different transition criteria often exist in parallel.

There has been considerable effort since the 1950s to map flow pattern boundaries for gas-liquid flow without swirl. This research culminated in a series of articles in the 1970s and 80s by Taitel, Dukler, Barnea, Mishima and Ishii (a.o.) in which transition criteria between patterns were proposed, based on a mechanistic modelling approach. Often, these start from a combination of existing correlations and flow idealizations to formulate a critical condition that separates two flow patterns. This critical condition is then reframed as a function of the superficial velocities (j_{G}, j_{L}) and plot against flow map data for verification. Figure 3.1 shows an example of this approach for an air-water system.

These criteria have been very successful in correctly predicting prevailing gas-liquid flow patterns based on given input conditions, and are still in widespread use today. The next section describes two transitions that are relevant to this thesis in more detail.

3.3 Example transition criteria for gas-liquid flow

3.3.1 Bubbly to slug transition

As illustrated in figure 2.1a, bubbly flow is characterized by a relatively homogeneous distribution of discrete bubbles in a continuous carrier liquid, that follow individual trajectories and do not interact much. A transition to slug flow can occur when these smaller bubbles cluster and coalesce into larger ones, and enough gas is present for these larger bubbles to keep increasing in size until they nearly bridge the pipe. The liquid phase then redistributes around and inbetween successive large bubbles, which attain their characteristic bullet shape (figure 2.1b).

Clustering and coalescence are promoted by a close proximity between bubbles. In a one-dimensional, statistically steady and developed bubbly flow, the proximity between bubbles is mainly determined by the total volume occupied by the gas, which is quantified by the volumetric fraction (α_{G}). Note that these flow conditions are emphasized here because in swirling flow, additional mechanisms (e.g. the centrifugal force) also influence the proximity between bubbles. As such, the transition criterion will generally be different.

From observations, multiple authors have deduced that the probability of bubble collisions strongly increases around a void fraction of 30 percent, whereas coalescence is rarely observed below 20 percent. This led Taitel and Dukler [3] to formulate the transition from bubbly to slug flow as a threshold condition on the average void fraction:

$$\widetilde{\alpha}_{\mathrm{G}} \;=\; 0.25 \tag{3.1}$$

This is a cross-sectional criterion, which they subsequently relate to the streamwise superficial velocity of both phases (flow rate per total area) by using the rise velocity of a single bubble in an infinite, quiescent liquid as a measure of the relative slip. They conclude that, at the transition,

$$j_{\mathrm{L}} \;=\; 3.0 j_{\mathrm{G}} - 1.15\left[\frac{\sigma g(\rho_{\mathrm{L}}-\rho_{\mathrm{G}})}{\rho_{\mathrm{L}}^2}\right]^{1/4} \tag{3.2}$$

At superficial liquid velocities j_{L} higher than given by equation (3.2) the flow will be bubbly, whereas at lower j_{L} slug flow will form.

Mishima and Ishii [5] use a threshold void fraction of 0.3, with a drift flux model in which the slip velocity between both phases is based on geometrical considerations, to formulate their transition criterion:

$$j_{\mathrm{L}} \;=\; \left(\frac{3.33}{C_0}-1\right) j_{\mathrm{G}} - \frac{0.76}{C_0}\left(\frac{\sigma g \Delta\rho}{\rho_{\mathrm{L}}^2}\right)^{1/4} \tag{3.3}$$

$$\text{where} \quad C_0 \;=\; 1.2 - 0.2\left(\frac{\rho_{\mathrm{G}}}{\rho_{\mathrm{L}}}\right)^{1/2} \quad \text{for circular pipes.}$$

Both (3.2) and (3.3) correctly distinguish the prevailing flow pattern in vertical gas-liquid flows over a wide range of experimental data [1].

Taitel and Dukler mention that bubbly flow can be sustained above $\widetilde{\alpha}_{\mathrm{G}} = 0.25$ whenever the turbulence intensity in the liquid phase is strong enough to break and disperse any larger bubbles formed. If, by this mechanism, the maximum bubble diameter remains below a critical size, coalescence is suppressed and slug flow cannot form. This scenario only occurs for high liquid flow rates, which Taitel and Dukler designate as *disperse bubbly flow*. From the critical bubble size, an additional criterion on the flow rates of both phases can be formulated to distinguish bubbly flow from slug flow at high liquid flow rates:

$$j_{\mathrm{L}} + j_{\mathrm{G}} \;=\; 4.0\left\{\frac{D^{0.429}(\sigma/\rho_{\mathrm{L}})^{0.089}}{\nu_{\mathrm{L}}^{0.072}}\left[\frac{g(\rho_{\mathrm{L}}-\rho_{\mathrm{G}})}{\rho_{\mathrm{L}}}\right]^{0.446}\right\} \tag{3.4}$$

When the mixture reaches the maximum allowable bubble packing (at $\widetilde{\alpha}_{\mathrm{G}} \sim 0.52$), the bubbly flow pattern cannot be sustained. Slug, churn or even annular flow result, depending on the flow rates of both phases.

3.3.2 Annular to churn transition

Annular flow is characterized by a broad, high velocity gas core surrounded by a thin liquid film that flows along the perimeter. In contrast to the other flow patterns in section 2.1 the gas phase is the continuous carrier: it forces the liquid film and any possible droplets entrained in the core upward by drag. A transition occurs when the gas velocity is not sufficient to overcome the gravitational forces on the liquid, which then accumulates upstream, blocking the pipe and causing the characteristic oscillatory motion associated with churn flow. This is quantified in different ways by leading authors.

Taitel and Dukler [3] proposed a transition criterion based on a simple force balance between gravity and drag for the maximum stable drop size in a turbulent gas flow:

$$\frac{j_{\mathrm{G}}\rho_{\mathrm{G}}^{1/2}}{\left(\sigma g(\rho_{\mathrm{L}}-\rho_{\mathrm{G}})\right)^{1/4}} \;=\; 3.1 \tag{3.5}$$

Their assumption is that the behaviour of the liquid film is similar to that of the entrained droplets. Notably, this criterion is independent of liquid flow rate and pipe diameter.[2]

Barnea [4] identified two possible mechanisms for the liquid to block the gas core, and formulated separate criteria to be satisfied in order for annular flow to exist:

1. *Flow reversal in the liquid film:* the effects of gas drag are most pronounced near the gas-liquid interface, whereas the gravitational forces on the liquid have equal magnitude throughout the film. This can result in a downward velocity near the wall, even though liquid near the interface flows upward. Barnea proposed a transition criterion based on a condition of neutral stability in the liquid film. It involves a simultaneous, iterative solving procedure for both superficial phase velocities and the equilibrium film thickness δ. For more detail on this procedure, the reader is referred to the corresponding article.

2. *Liquid bridging:* if the liquid flow rate is high enough, the equilibrium film thickness is such that interfacial waves on both sides can form a bridge across the pipe. This liquid bridge can to a certain extent be aerated with gas bubbles, which implies that this mechanism can cause transition for lower liquid holdup than intuitively expected. Barnea set this transition criterion as $\widetilde{\alpha}_{\mathrm{G}} \geq 0.24$.

3.4 Application to swirling flow

The examples of the previous section illustrate that, with smart modelling assumptions, the fundamental behaviour of a gas-liquid flow can be distilled into a series of concise criteria, which together pinpoint the prevailing flow pattern for given input conditions. Even though this modelling approach is only approximate, its results have proven reliable for many practical purposes [25].

Conceptually, the transition criteria developed for gas-liquid flow without swirl can be thought to revolve around two quantities: a measure of the distribution of phases (α), and the applied pressure gradient (the driving force that enforces the flow rates). These two quantities are interrelated because α determines the distribution of weight over the cross section, which influences the local velocities that can be achieved for a given pressure gradient. In turn, the distribution of velocities leads to an adjustment of α. In order to extend the mechanistic modelling approach to swirling flow, an understanding is required of how the swirling motion affects these quantities.

A swirling flow is characterized by the presence of a tangential velocity component u_θ. This is the source of a radial pressure gradient that induces an inward 'buoyancy' on the

---

[2] The physical basis for this transition has been disproven in recent PhD research. This criterion still has widespread use in practice, but works for the wrong reasons [22].

lighter phase of a mixture flow. As a result, the phases are non-homogeneously distributed over the cross section, as is visually apparent from the observations discussed in chapter 2. From a modelling perspective, the magnitude of u_θ affects the parameter α.

However, the swirling motion also affects the driving pressure gradient, through its decay. This is not as clear from observations, but follows from the equality of cross derivatives. The radial pressure gradient degrades with downstream distance (z) through the influence of shear stresses at the pipe wall on u_θ. As a consequence, a radial variation of the driving pressure gradient is implied by:

$$\boxed{\frac{\partial}{\partial z}\left(\frac{\partial p}{\partial r}\right) = \frac{\partial}{\partial r}\left(\frac{\partial p}{\partial z}\right)} \tag{3.6}$$

This is in strong contrast the criteria discussed above, which are based on fully developed, one-dimensional flow. Here, the axial pressure gradient is constant over the entire cross section. Swirling flows are distinctly three-dimensional by nature, and allow only for limited idealizations without sacrificing essential physics involved. If significant, radial variations of the axial pressure gradient therefore have to be considered when modelling.

The influence of u_θ on α and the distribution of the pressure gradient can vary however, depending on its local magnitude and downstream evolution. The relative magnitude of the derivatives $\partial/\partial r$ and $\partial/\partial z$ is therefore a key aspect in modelling of swirling flows: this is indicative of the importance of variations in α and the axial pressure gradient for a correct prediction of the flow dynamics. This is further elaborated on in chapter 4.

High and low gas limits

It is noted here that a mechanistic model may be easier to formulate in asymptotical or limit situations, where the dominant underlying mechanisms tend to be most clear. In gas-liquid flows without swirl, bubbly and annular flow are relatively stable patterns with well-understood boundaries. Slug and churn flows on the other hand, feature complicated dynamics, unclear transitions, and understanding these often requires a combination of disperse and separated flow models or matching asymptotical solutions at their boundaries. By analogy, a sensible approach to modelling swirling flows would be to start from a low gas or high gas limit.

Currently, several researchers are focused on swirling annular flow (high gas limit) and modifying the transition criteria formulated by Barnea to include the effects of swirl [8, 14]. In this thesis, an attempt is made to establish a modelling framework for swirling gas-liquid flow in the low gas limit. This is of fundamental interest because at these operating conditions, the most notable pattern transition takes place, i.e. bubbly to columnar flow. Also, the TOMOCON flow loop can be used in this range to verify model predictions, whereas it cannot provide the high gas rates required for annular flow. In the next chapter, the modelling framework and its underlying assumptions are set out.

PART 2

Modelling

Chapter 4

Modelling framework

This chapter establishes a conceptual modelling framework for swirling gas-liquid flow based on the two-fluid model, with interrelated balance equations for each phase [25]. A number of modelling assumptions are put forward that allow for simplification of the governing equations to make the problem analytically tractable. Section 4.1.4 features a simplified set of equations for the mean flow, in which only relevant terms are retained. These equations form the basis for the iterative solving routine described in section 4.2.

4.1 Governing equations

In continuum mechanics, flow is considered as the continuous deformation of a fluid under the influence of stresses. This behaviour is determined by a set of conservation equations for mass and momentum[1], which in their general form are given by [27]

$$\text{mass:} \qquad \frac{\partial \rho}{\partial t} + \frac{\partial}{\partial x_j}\big(\rho u_j\big) = 0 \tag{4.1}$$

$$\text{momentum:} \qquad \rho\frac{\partial u_i}{\partial t} + \rho u_j\frac{\partial u_i}{\partial x_j} = \rho g_i - \frac{\partial p}{\partial x_i} + \frac{\partial \tau_{ij}}{\partial x_j} \tag{4.2}$$

The momentum balance holds per coordinate direction. Here, τ_{ij} is the deviatoric part of the stress tensor, which requires a closure relation in order to solve a specific flow problem.

In multiphase flow these equations can be used for a mixture density $\widetilde{\rho}$, but <u>only</u> if there is no relative motion between the phases. In general however, each phase satisfies its own conservation equations, which are weighted by the volumetric fraction it occupies within the mixture. This is represented for phase N by parameter α_{N}, with a 0-1 range [23]:

$$\frac{\partial}{\partial t}\big(\alpha_{\text{N}}\rho_{\text{N}}\big) + \frac{\partial}{\partial x_j}\big(\alpha_{\text{N}}\rho_{\text{N}}u_{\text{N}j}\big) = 0 \tag{4.3}$$

$$\alpha_{\text{N}}\rho_{\text{N}}\frac{\partial u_{\text{N}i}}{\partial t} + \alpha_{\text{N}}\rho_{\text{N}}u_{\text{N}j}\frac{\partial u_{\text{N}i}}{\partial x_j} = \alpha_{\text{N}}\rho_{\text{N}}g_i - \alpha_{\text{N}}\frac{\partial p}{\partial x_i} + \mathcal{F}_{\text{N}i} + \frac{\partial \tau_{\text{N}ij}}{\partial x_j} \tag{4.4}$$

It follows that the sum of all volumetric fractions equals unity and hence the mixture density is defined as $\widetilde{\rho} = \sum\alpha_{\text{N}}\rho_{\text{N}}$. Additionally, the individual phase momentum equation accounts for the possibility of momentum transfer between phases, through their shared interface, via the force interaction term $\mathcal{F}_{\text{N}i}$. This requires additional modelling, which is treated in further detail in section 4.1.3.

---

[1] For the modelling framework developed in this thesis, the energy conservation equation is not of relevance. It is therefore not treated in the main text.

The general form of these equations changes upon accounting for the effects of geometry, flow idealizations and turbulence, as illustrated in the following sections.

Geometry

The modelling framework is based on gas-liquid flow in a vertically oriented, circular pipe. For analytical clarity, the pipe is assumed to be infinite in the streamwise direction, with a swirling motion prescribed at a given reference level. This allows for focus on the effects of a certain swirl rate, and avoids practical complications associated with the generation of swirl, input flow development, etc.

This geometry is best described in cylindrical coordinates (r, θ, z) with the streamwise coordinate axis aligned with the centerline of the pipe, as illustrated in figure 4.1. In addition, a wall-normal coordinate y is defined for modelling quantities that scale with the distance from the wall. The possible ranges of these coordinates are:

$$\begin{aligned} r &: [\,0, R\,] \\ \theta &: [\,0, 2\pi) \\ z &: (-\infty, \infty) \\ y &: [\,0, R\,] \end{aligned}$$

Velocities are indicated with the letter u for the liquid phase, and v for the gas phase. Gravity is directed along the negative streamwise direction, i.e. $g_i = (0, 0, -g)$.

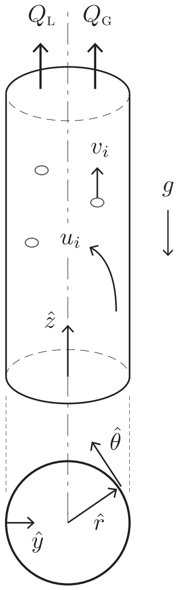

Figure 4.1

4.1.1 Flow idealizations

The following assumptions are made to idealize the swirling flow:

1. *Incompressible flow:* fluid densities are not assumed to vary with pressure. In practice, such variations are on the order of a few percent only for most pipe flows.

2. *Statistically steady:* for a turbulent flow, this implies that the mean flow is constant in time and the time derivative of its fluctuations averages to zero over successive measurements [26]. One can still account for transient dynamics (e.g. slug and churn flows) on the basis of streamwise translations, using the ergodicity hypothesis [27].

3. *Axisymmetry:* in non-swirling flow, the symmetry of the pipe geometry extends to the velocity profile, which is independent of θ. In swirling flow, the additional velocity component u_θ results in a helical fluid motion. The velocity field is now symmetrical along planes of constant $\theta - z/l$, where l is related to the pitch of the helical flow [17].

   Although expressions for the governing equations in a helical coordinate basis exist, these greatly complicate calculations. Instead, it is assumed here that the swirling flow maintains axisymmetry, and $\partial/\partial\theta$ of any quantity equals zero. If velocity components do not change significantly over the streamwise distance traveled by one helical revolution (see 5.) this assumption is legitimate, as for any function f expansion of the mixed-coordinate derivative by the chain rule yields

$$\frac{\partial f}{\partial(\theta - z/l)} \;=\; \left(\frac{\partial}{\partial\theta} - l\,\frac{\partial}{\partial z}\right) f \;\approx\; \frac{\partial f}{\partial\theta}$$

4. *Negligible radial velocity:* in fully developed, one-dimensional flow, u_r equals zero everywhere as a consequence of continuity. In swirling flow, the radial velocity is generally nonzero, but expected to be small in cases of limited streamwise variation.

Previous numerical simulations of swirling single-phase pipe flow have pointed out that u_r is at least $\mathcal{O}(10^{-3})$ smaller than u_θ, u_z [33]. It is assumed here that this result can be generalized to gas-liquid flows, at least in the low gas limit.

5. *Negligible streamwise derivatives:* there is streamwise variation of all relevant quantities in a swirling flow, as a consequence of its decay with axial distance. However, for relatively limited decay rates (or high local rotation rates) it can be assumed that these are negligible in comparison to variations in the radial direction, i.e.

$$\frac{\partial}{\partial z}(...) \ll \frac{\partial}{\partial r}(...)$$

Using scaling arguments, Reynolds estimated the ratio between streamwise and radial variations as 1 : 50 in swirling pipe flow [18]. He states that this condition is *implied* when requiring both axisymmetry and radial equilibrium for swirling flows.

The above assumption is representative of a quasi-1D approach to modelling, where changes in the streamwise direction are gradual enough to ignore their effect on the dynamics in the cross section. This allows for calculating the latter as a series of successive equilibrium states first, and only afterward solve for their evolution, as a one-dimensional problem in z. Section 4.2.4 will further expand on the use and validity of this approach in the iterative solving procedure.

4.1.2 Turbulence modelling

The swirling flow inside a separator is turbulent under practical operating conditions, with Reynolds numbers of order $10^4 - 10^5$ for most gas-liquid mixtures. Turbulent flow is characterized by a chaotic motion of entangled, irregular vortex-like flow structures of different sizes (*eddies*), that cause continuous fluctuations of all relevant quantities in both time and space. These fluctuations have a large influence on the dynamics of the flow, increasing its frictional losses, but also enhancing its mixing and transfer rates, among other effects [27].

Resolving the instantaneous details of a turbulent flow requires a numerical approach and vast computational resources. For the purpose of constructing a simplified modelling framework for real-time control however, a *statistical approach* to turbulence is more suitable. This approach, initially developed by Reynolds, investigates the evolution of the mean and the standard deviation of all flow quantities rather than their instantaneous values. These statistics are obtained by averaging over multiple realizations of a turbulent flow for given input conditions. This is known as ensemble averaging. Reynolds' statistical approach greatly reduces the complexity of a turbulent flow problem and allows for its analytical study, at the cost of sacrificing detail. Its benefits cannot be overstated: to a great extent, the theoretical framework of turbulent flows was developed using the statistical approach. Its use is also prevalent in industrial applications [27].

For swirling gas-liquid flow, the relevant quantities to decompose into their mean and fluctuating parts are velocity and pressure:

$$\begin{aligned} u_i &= U_i + u_i' \\ v_i &= V_i + v_i' \\ p &= P + p' \end{aligned} \tag{4.5}$$

Mean quantities are indicated by a capital letter and fluctuations with a prime. Ensemble averaging of any term is represented by an overbar. By definition, the ensemble average of the mean is the mean itself, and that of the fluctuations equals zero.

Substitution of the decomposed quantities and subsequent averaging of the conservation equations of mass and momentum yield the equations for the mean flow. While there is a strong similarity to (4.1) and (4.2), the momentum equation features additional terms of the form $\rho\overline{u_i'u_j'}$. These are correlations between velocity fluctuations, that do not average to zero because the three-dimensional dynamics of turbulent eddies prevent any pair of fluctuations from being fully statistically independent. These terms represent fluxes of momentum and are often referred to as turbulent 'stresses' because they affect the behaviour of the mean flow in the same way surface stresses do. As such, it is common to define the total deviatoric stresses in a turbulent flow as:

$$\tau_t \;=\; -\rho\overline{u_i'u_j'} + \mu\left(\frac{\partial U_i}{\partial x_j} + \frac{\partial U_j}{\partial x_i}\right) \tag{4.6}$$

Boussinesq closure hypothesis

It is important to note that the turbulent stresses are not due to dissipative effects at the molecular level, but stem from the nonlinear interaction between velocity components in the advective term. The turbulent stresses therefore scale with the mean flow, i.e. with the inertial forces. As a consequence, each term in equation (4.6) dominates over the other in a different region of the flow domain: turbulent stresses are large in the center of the flow, where viscous stresses are negligible due to the absence of strong gradients. Very near the wall, where there is limited flow, turbulent stresses approach zero while viscous stresses strongly increase in magnitude.

Even though their origin differs, Boussinesq formulated a closure hypothesis for modelling the turbulent stress tensor in analogy to Newton's law of viscosity. It assumes that $\overline{u_i'u_j'}$ is similarly proportional to the mean strain rate, with a scalar proportionality parameter referred to as the *eddy viscosity*:

$$-\overline{u_i'u_j'} + \frac{1}{3}\overline{u_k'^2}\,\delta_{ij} \;=\; \nu_t\left(\frac{\partial U_i}{\partial x_j} + \frac{\partial U_j}{\partial x_i}\right) \tag{4.7}$$

This hypothesis is crude, but has appeared to provide realistic results for simple geometries. Note that ν_t is not a material constant, but depends on the local flow conditions. In wall-bounded flows, it is usually estimated on the basis of Prandtl's *mixing length hypothesis*:

$$\nu_t \;=\; L^2\left|\frac{\partial U}{\partial y}\right| \tag{4.8}$$

The 'mixing length' L is a characteristic length scale of an eddy in the local flow. It has a different definition in each region of the flow. Near the centerline for example, eddies scale with the size of the flow domain, whereas in the wall region the maximum eddy size is limited by its distance to the wall.

An important theoretical result obtained by using this approach is the analytical expression for the mean velocity profile in turbulent pipe flow. These expressions are shortly summarized and elaborated on in the next section, as some aspects can be generalized for use in the case of swirling gas-liquid flow.

Other, sophisticated closure models for the turbulent stresses exist, that provide more accurate results over a wider range of geometries (e.g. the k–ε model). However, to keep a clear modelling framework for swirling flow with minimal assumptions, the above hypotheses are deemed sufficient for proper first-order estimates of the relevant quantities.

Turbulent pipe flow velocity profile (single-phase)

Under the Boussinesq hypothesis, equation (4.6) can be used to resolve the mean velocity profile from knowledge of the total stresses at a point in the flow. These local stresses are often expressed in practice as a function of their magnitude at the wall. For turbulent flow, it is common to express the wall shear stress as:

$$\tau_t(R) \;=\; \rho u_*^2 \tag{4.9}$$

Here, u_* is a characteristic velocity scale referred to as the *friction velocity.* For a fully-developed flow, u_* can be related to the driving pressure gradient by a balance of forces over the pipe cross section:

$$u_*^2 \;=\; \frac{R}{2}\left(-\frac{2}{\rho R^2}\int_0^R \frac{\partial P}{\partial z}\, r\,\mathrm{d}r \,-\, g\right) \tag{4.10}$$

Experimental observations of the behaviour of τ_t throughout the flow have led to a subdivision of the pipe into several regions. Each of these has a different expression for the corresponding eddy viscosity ν_t and velocity profile $U_z(r)$. This is summarized in table 4.1 and figure 4.2. Further detail on these derivations exceeds the scope of this thesis. Instead, one can refer to one of many standard text books on turbulence, e.g. [26, 27].

In all regions except very near the wall, viscous stresses are negligible. In the buffer layer, both contributions to τ_t are relatively equal in magnitude and it is not possible to derive an analytical expression for U_z. Observations indicate that the velocity profile here transitions smoothly between the viscous sublayer and logarithmic layer solutions. Several fitting functions exist that can be used in the buffer layer for estimation of the velocity.

The relative size of these regions is ultimately dependent on the Reynolds number of the flow. Their range is therefore expressed in non-dimensional units from the wall, using the friction velocity and viscosity:

$$y^+ \;=\; \frac{u_* y}{\nu} \tag{4.11}$$

The velocity profiles in the logarithmic layer and viscous sublayer are notable for being independent of the flow geometry. The observed behaviour in these regions is *universal* to all wall-bounded flows and therefore referred to as the ‘law of the wall’. In particular, it has been indicated by Kitoh that even in swirling flows the law of the wall is relatively unaffected [15], a result that will be employed in section 4.2.3.

core $r < 0.43\,D$	$\nu_t = \left(\beta R\right)^2 \left\lvert\frac{\partial U}{\partial y}\right\rvert$	$U_z = U_1 \,-\, \frac{2}{3}\frac{u_*}{\beta}\left(\frac{r}{R}\right)^{3/2}$
logarithmic layer $20 \lesssim\, y^+ \lesssim 100$	$\nu_t = \;\left(k\,y\right)^2 \left\lvert\frac{\partial U}{\partial y}\right\rvert$	$U_z = u_*\left(\frac{1}{k}\ln\!\left(\frac{u_* y}{\nu}\right) + 5.0\right)$
buffer layer $5 \lesssim\, y^+ \lesssim 20$	–	–
viscous sublayer $y^+ \lesssim 5$	$\nu_t \ll \nu$	$U_z = \frac{u_*^2}{\nu}\,y$

Table 4.1: Summary of single-phase, turbulent pipe flow regions and their corresponding expressions for the eddy viscosity (ν_t) and mean velocity (U_z), obtained using the Boussinesq closure hypothesis. $\beta \approx 0.13$ for pipe flow, $k = 0.4$.

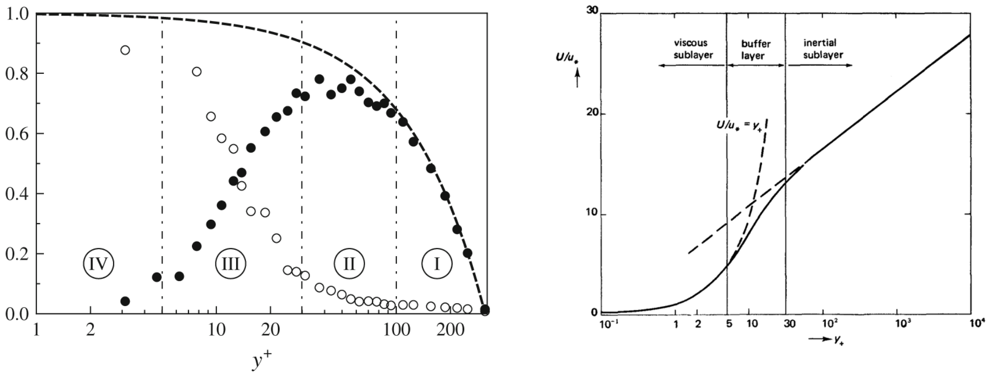

(a) viscous and turbulent (open/solid) stress distributions, normalized by the wall shear stress. I: core, IV: viscous sublayer

(b) velocity profile in the wall region — viscous sublayer and log layer solutions match at $y^+ \approx 11$.

Figure 4.2: Single-phase turbulent pipe flow characteristics: the distribution of stresses over the pipe cross section and the universal velocity profile in the wall region ('law of the wall'). *reprints from* [27, 26]

4.1.3 Interfacial momentum transfer

Momentum transfer between various phases of a multiphase flow is due to surface forces exerted by each fluid on their shared interface. For regular gas-liquid flows in the low gas limit, section 2.1 illustrated that the phases settle into a configuration of discrete bubbles dispersed throughout a continuous carrier liquid. (The shared interface is this case is formed by the sum of all bubble surfaces.) If these bubbles are small in relation to the characteristic scales of the flow, it is customary to represent the gas phase as a collection of non-interacting point particles. Each of these resides in its own 'infinite medium' of flow properties as they are *at the position of the particle.* This local flow is quantified by a particle Reynolds number, based on the particle diameter and local relative velocity:

$$\mathrm{Re}_p \;=\; \frac{\left|\vec{v}-\vec{u}\right| d}{\nu_{\mathrm{L}}} \tag{4.12}$$

The total force exerted on a particle by its local flow is representative of the change in momentum it experiences. There can be various force mechanisms involved, which generally have a complex dependence on both the instantaneous flow and its history. Of relevance to this thesis are the effects of drag and lift, under the flow conditions set in section 4.1.1. These are elaborated on in the subsections below. An in-depth treatment of other force mechanisms can be found in the literature [23].

An important simplification in this approach is that all contributing force mechanisms are calculated separately and then superposed to obtain the total particle force:

$$\vec{F} \;=\; \vec{F}_{\mathrm{D}} + \vec{F}_{\mathrm{L}} + \ldots$$

Where applicable, these contributions are linearised in the relative velocity term. This avoids any analytical complications that arise from nonlinearities and allows for studying each coordinate direction separately.

Under these assumptions, the total interfacial momentum transfer towards the gas phase equals F multiplied by the number of bubbles, which can be obtained by dividing the volume fraction α_{G} by the volume of one bubble:

$$\left\langle \mathcal{F}_{\mathrm{G}i} \right\rangle \;=\; \alpha_{\mathrm{G}} \frac{\left\langle F_i \right\rangle}{\pi d^3/6} \tag{4.13}$$

The averaging operators in (4.13) account for the possibility of bubbles in different regions of local flow to experience a different particle force.

Coupling and limit behavior in swirling gas-liquid flow

In disperse flow reasoning, the forces associated with a single particle are usually of little influence to the local flow. However, collective motions and clustering of the disperse phase may affect the turbulence in the carrier fluid, and thereby reduce or enhance the forces on each particle. This feedback mechanism is particularly noticeable if the volume fraction of the disperse phase is large or very localized in space. If its effects are of significant influence on the interfacial momentum transfer, the flow is said to be *two-way coupled.*

In gas-liquid flows with low gas content, *one-way coupling* is most prevalent. There is no significant feedback from the gas phase and the total interfacial momentum transfer is negligible for the liquid phase in comparison to the other terms in the momentum equation, since $\alpha_{\mathrm{G}} \sim 0$ on average. If the flow is swirling however, the non-homogeneous distribution of the gas phase does not necessarily legitimize this reasoning in local flow regions. Rather, the interfacial momentum transfer will change in regions of enhanced gas concentration, as there is less carrier fluid per unit volume in the surroundings to exert forces on the bubbles. In the limit of very high gas fraction, these forces should approach zero.

A simple approach to modelling this effect without invoking the complications of two-way coupling, is to multiply the contributing forces by α_{L}. This produces the correct limit behaviour, and other modelling attempts for gas-liquid flows in the literature have shown favorable results using this approach [16]. It is employed in the following sections.

Drag

The drag force exerted on a spherical particle by its local flow is due to a relative velocity between them. This is also referred to as *slip.* In linearised form, it is expressed as

$$F_{\mathrm{D}i} \;=\; -\frac{1}{2}\frac{\pi d^2}{4} C_{\mathrm{D}} \alpha_{\mathrm{L}} \rho_{\mathrm{L}} \big|\vec{v} - \vec{u}\big| \big(v_i - u_i\big) \tag{4.14}$$

Here, $\big|\vec{v} - \vec{u}\big|$ is a measure of the characteristic magnitude of the slip velocity. As per the previous section, a dependence on α_{L} is factored in to account for the required limit behaviour in regions of high particle concentration. A suitable correlation for the drag coefficient C_{D} should be provided, for which several expressions exist in the literature.

The average contribution of drag to the interfacial momentum transfer towards the gas phase follows from substitution of (4.14) into (4.13). If both velocities are decomposed into their mean and fluctuating parts, this yields:

$$\big\langle \mathcal{F}_{\mathrm{G}i} \big\rangle_{\mathrm{D}} \;=\; -\alpha_{\mathrm{G}} \cdot \frac{3}{4}\frac{C_{\mathrm{D}}}{d} \alpha_{\mathrm{L}} \rho_{\mathrm{L}} \big|\vec{v} - \vec{u}\big| \Big\langle V_i + v_i' - \big(U_i + u_i'\big) \Big\rangle \tag{4.15}$$

The terms inside the averaging operator require further consideration. Naturally, a difference between the mean velocities V_i and U_i causes particle drag and so contributes to the interfacial transfer of momentum. However, even in cases of zero mean drag there can be a contribution from the average of the velocity fluctuations of the continuous phase (u'), which do not necessarily equal zero when calculated at the position of the particle.[2] This mechanism is called *turbulent dispersion.*

Turbulent dispersion occurs in situations where a non-homogeneous distribution of particles exists, which is agitated by a fluctuating local flow velocity, e.g. in an eddy. Even though the fluid displacements in either direction might equal, this results in a net transport of particles away from the region of higher concentration. Because this alters the average

---

[2] The velocity fluctuations *of* the particle are defined relative to the position of the particle at any given time. Therefore $\langle v' \rangle = 0$, as per the general definition of Reynolds decomposition.

particle direction of motion, there has to be momentum transfer from the continuous to the disperse phase. Note that agitation is essential: for example, regions of enhanced particle concentration very near a pipe wall (where $u' \sim 0$) tend to remain stable, even though these can be initially caused by turbulent dispersion away from the core flow.

Transport induced by concentration differences is often quantified with a *gradient diffusion model*, of which Fick's law is a well-known example. In multiphase flow, the equivalents to concentration are the volumetric fractions. Therefore, the turbulent dispersion mechanism can be modelled as [28]

$$\left\langle u_i' \right\rangle \;=\; -\mathbb{D}_t \left(\frac{1}{\alpha_{\mathrm{G}}} \frac{\partial \alpha_{\mathrm{G}}}{\partial x_i} - \frac{1}{\alpha_{\mathrm{L}}} \frac{\partial \alpha_{\mathrm{L}}}{\partial x_i} \right) \tag{4.16}$$

Here, $\mathbb{D}_t$ is a turbulent dispersion coefficient. The Reynolds analogy asserts that transport coefficients for all quantities transported by a turbulent flow are roughly equal, as they all depend on mixing by eddies. It is therefore customary to write

$$\mathbb{D}_t \;=\; \frac{\nu_t}{\mathrm{Sc}} \tag{4.17}$$

where Sc is a turbulent Schmidt number of $\mathcal{O}(1)$ that captures the difference between mass and momentum transfer [28]. It can be used in practice as a fit parameter to match experimental data. By using the mutual dependence of volumetric fractions $\alpha_{\mathrm{L}} = 1 - \alpha_{\mathrm{G}}$, equation (4.16) can be rewritten to

$$\left\langle u_i' \right\rangle \;=\; -\frac{\mathbb{D}_t}{\alpha_{\mathrm{G}} \alpha_{\mathrm{L}}} \frac{\partial \alpha_{\mathrm{G}}}{\partial x_i} \tag{4.18}$$

In the absence of mean drag then, the average interfacial momentum transfer reduces to:

$$\left\langle \mathcal{F}_{\mathrm{G}i} \right\rangle_{\mathrm{D}} \;=\; -\frac{3}{4} \frac{C_{\mathrm{D}}}{d} \rho_{\mathrm{L}} \left| \vec{v} - \vec{u} \right| \mathbb{D}_t \frac{\partial \alpha_{\mathrm{G}}}{\partial x_i} \tag{4.19}$$

Lift

The lift force exerted on a spherical particle by its local flow is due to the interplay between the particle direction of motion and the circulation of the local flow field:

$$F_{\mathrm{L}i} \;=\; -\frac{\pi d^3}{6} C_{\mathrm{L}} \alpha_{\mathrm{L}} \rho_{\mathrm{L}} \Big(\left(\vec{v} - \vec{u} \right) \times \left(\nabla \times \vec{u} \right) \Big)_i \tag{4.20}$$

The resultant force is perpendicular to the local flow direction. Again, a dependence on α_{L} is factored in to reduce lift in regions of less fluid surrounding the particle. The lift coefficient C_{L} tends to vary significantly with particle shape, and different correlations accounting for this effect exist in the literature.

For a more intuitive understanding of the effect of lift on the particle trajectory, the cross products can be worked out under the assumptions made in section 4.1.1. The curl of the local flow field then becomes

$$\nabla \times \vec{u} \;=\; -\frac{\partial u_\theta}{\partial z} \hat{r} - \frac{\partial u_z}{\partial r} \hat{\theta} + \left(\frac{\partial u_\theta}{\partial r} + \frac{u_\theta}{r} \right) \hat{z} \tag{4.21}$$

Now, it is assumed that the average slip velocity between the particle and the flow is directed along the streamwise direction only, i.e. $\langle \vec{v} - \vec{u} \rangle = U_0 \, \hat{z}$. For most vertical gas-liquid flows, with a density ratio $\rho_{\mathrm{G}} / \rho_{\mathrm{L}} \ll 1$ and therefore large differences in buoyancy between both phases, this is expected to be at least the dominant contribution. In this case, the total cross product in equation (4.20) simplifies to

$$\Big\langle \left(\vec{v} - \vec{u} \right) \times \left(\nabla \times \vec{u} \right) \Big\rangle \;=\; U_0 \left(\frac{\partial U_z}{\partial r} \hat{r} - \frac{\partial U_\theta}{\partial z} \hat{\theta} \right) \tag{4.22}$$

Equation (4.22) explicitly shows the lift force acts perpendicular to the local flow direction. If effects of swirl decay are ignored, as in the quasi-1D approach outlined in section 4.1.1, the resultant force is along the radial direction only. Substitution of (4.20) into (4.13) yields the following expression for the average interfacial momentum transfer in the radial direction due to lift:

$$\left\langle \mathcal{F}_{\mathrm{G}r} \right\rangle_{\mathrm{L}} = -\alpha_{\mathrm{G}} \alpha_{\mathrm{L}} \rho_{\mathrm{L}} C_{\mathrm{L}} U_0 \frac{\partial U_z}{\partial r} \tag{4.23}$$

If the streamwise velocity profile $U_z(r)$ has its maximum at the centerline and decreases monotonically for increasing r, as are e.g. both the laminar and turbulent velocity profiles in one-dimensional pipe flow, the lift force is directed *outward* from the center. This can lead to a strong increase of particle concentration in the near-wall region, where velocity gradients are high, as multiple authors have pointed out to explain observations [11, 13].

In swirling flow, single-phase experimental data indicate that $U_z(r)$ tends to decrease in the core of the flow, towards a minimum at the centerline [15, 31, 32]. In this case, the lift force is directed *inward*.

4.1.4 Simplified equations for the mean flow

With the theoretical basis developed in the previous sections, the conservation equations of mass (4.3) and momentum (4.4) can now be recast into a form specific to swirling gas-liquid flow in a vertical pipe. Our interest lies in the core flow region, because the swirling motion promotes a separation of phases near the centerline. The equilibrium distribution of the mean flow quantities here is important for studying possible transition mechanisms from bubbly to columnar flow. As a corollary, the effects of viscosity are neglected in the equations below.

The conservation equation of mass has no useble form as all terms drop out under the assumptions made. The momentum equation, specified per coordinate direction and with only relevant terms retained, reduces to:

$$r: \qquad -\alpha_{\mathrm{N}} \rho_{\mathrm{N}} \frac{U_{\mathrm{N}\theta}^2}{r} = -\alpha_{\mathrm{N}} \frac{\partial P}{\partial r} + \left\langle \mathcal{F}_{\mathrm{N}r} \right\rangle - \frac{1}{r} \frac{\partial}{\partial r} \left(r \, \alpha_{\mathrm{N}} \rho_{\mathrm{N}} \overline{u'^2_{\mathrm{N}r}} \right) - \frac{\overline{u'^2_{\mathrm{N}\theta}}}{r} \tag{4.24}$$

$$\theta: \qquad 0 = \left\langle \mathcal{F}_{\mathrm{N}\theta} \right\rangle - \frac{1}{r^2} \frac{\partial}{\partial r} \left(r^2 \, \alpha_{\mathrm{N}} \rho_{\mathrm{N}} \overline{u'_{\mathrm{N}\theta} u'_{\mathrm{N}r}} \right) \tag{4.25}$$

$$z: \qquad 0 = -\alpha_{\mathrm{N}} \rho_{\mathrm{N}} g - \alpha_{\mathrm{N}} \frac{\partial P}{\partial z} + \left\langle \mathcal{F}_{\mathrm{N}z} \right\rangle - \frac{1}{r} \frac{\partial}{\partial r} \left(r \, \alpha_{\mathrm{N}} \rho_{\mathrm{N}} \overline{u'_{\mathrm{N}z} u'_{\mathrm{N}r}} \right) \tag{4.26}$$

For the interfacial momentum transfer terms, any combination of the expressions obtained in section 4.1.3 can be substituted.

These equations form the basis for the iterative solving routine described in the next section. A full set of expanded equations, including all terms discarded here, is available for reference in appendix A.

4.2 Solving routine

This section outlines an iterative solving routine to estimate the quantities that determine the prevalent flow pattern in swirling gas-liquid flow. Because of the complex dynamics of the swirling motion and the interdependency of its associated parameters, it pays to first formulate our objective in clear terms, in relation to the simplified conservation equations. Also, the input flow is considered in more detail prior to estabilishing the routine.

Objective

From the visual observations discussed in chapter 2, it follows that a swirling flow problem is uniquely framed by a combination of three parameters (j_{L}, j_{G}, Ω):

- The superficial velocities (j_{L}, j_{G}) are indicative of the availability of liquid and gas in any given cross section. Additionally, they provide a measure of the net forcing that drives the flow. In the low gas limit, the latter mainly applies to j_{L} — the gas phase behaviour is to a large extent prescribed by the liquid.
- The swirl number Ω is a measure of the intensity of swirling motion obtained for a certain input flow. It represents the non-dimensionalized flux of angular momentum in the axial direction [15]. It is fixed by the geometry of the swirl-inducing mechanism, e.g. by the angle of the vanes in an axial cyclone.

A flow map reflects this: it is constructed for a setup with certain Ω, and allows for pinpointing the prevailing flow pattern based on any given combination of (j_{L}, j_{G}).

In the simplified conservation equations (4.24)–(4.26), these parameters do not occur naturally. It is therefore proposed to use a related, but more suitable combination:

$$\text{input} \quad \left(\frac{\partial P}{\partial z},\, j_{\mathrm{G}},\, U_\theta\right) \quad \longrightarrow \quad \left(U_0,\, U_z,\, \alpha_{\mathrm{G}},\, \alpha_{\mathrm{L}}\right) \quad \text{output}$$

The axial pressure gradient replaces j_{L} because it is a direct input to the z-momentum equation. Also, section 3.4 illustrated that it can have a radial dependence when swirl decay is considered, which may influence the distribution of all quantities. In contrast, j_{L} is an averaged parameter, in which such information is discarded. U_θ is used as a measure of swirling motion as it is directly linked to the centripetal forces exerted on the fluid mixture.

The output quantities obtained through the conservation equations are: the slip velocity between both phases U_0, the streamwise velocity profile $U_z(r)$, and the radial distribution of volumetric fractions (α_{G}, α_{L}). Expressions for these quantities are detailed in dedicated subsections below. Note that the superficial gas velocity j_{G} remains an input parameter, because the available gas yields an integral limit on the volumetric gas fraction α_{G}:

$$j_{\mathrm{G}} \;=\; \frac{1}{\pi R^2} \iint \alpha_{\mathrm{G}} \left(U_z + U_0\right) r \,\mathrm{d}r \,\mathrm{d}\theta \tag{4.27}$$

Equation (4.27) is used to find the proper scaling for α_{G}. After convergence of the solving routine, j_{L} and Ω can be calculated from the output quantities[3] by the following relations:

$$j_{\mathrm{L}} \;=\; \frac{1}{\pi R^2} \iint \alpha_{\mathrm{G}} U_z \, r \,\mathrm{d}r \,\mathrm{d}\theta \tag{4.28}$$

$$\Omega \;=\; \frac{1}{\pi R^3 j_{\mathrm{L}}^2} \iint U_\theta \, U_z \, r^2 \,\mathrm{d}r \,\mathrm{d}\theta \tag{4.29}$$

Now, with (j_{L}, j_{G}, Ω) from the modelling framework, it becomes possible to investigate the relation between the calculated distributions (α_{G}, α_{L}) and the flow patterns observed in maps for the same Ω. This should prove insightful for formulating transition criteria from bubbly to columnar flows.

Input flow

It is assumed that the flow upstream (before acquiring its swirling motion) is bubbly, with gas bubbles distributed homogeneously throughout the cross section. It is fully developed due to the infinite lead-up and both phases are in equilibrium. This implies that gas and liquid mean velocity components are equal when there is no slip between them.

A slip velocity U_0 is only taken into account along the streamwise direction. For vertical gas-liquid flows, with a density ratio $\rho_\mathrm{G}/\rho_\mathrm{L} \ll 1$ and therefore large differences in buoyancy between both phases, this is expected to closely reflect reality. The addition of swirling motion does not change the orientation of the slip velocity, but may affect its magnitude. Hence, when calculating any equilibrium situation after swirl is applied, mean velocity components of the gas and liquid phase are related by:

$$\begin{aligned} V_r &= U_r \sim 0 \\ V_\theta &= U_\theta \\ V_z &= U_z + U_0 \end{aligned}$$

4.2.1 Slip velocity

To estimate the slip velocity, the z-momentum equation for the gas phase (4.26) is used. Interfacial momentum transfer is primarily due to drag: it is modelled by using equation (4.15) for the mean velocities only, while ignoring the fluctuations. Turbulent stresses in the gas phase are assumed to be negligible, which is a common approximation for bubbly flows. This approach mirrors the reasoning of Laviéville et al. in their modelling of a similar problem for bubbly flow without swirl [13]. The resultant balance equation reads:

$$0 = -\alpha_\mathrm{G}\rho_\mathrm{G} g - \alpha_\mathrm{G}\frac{\partial P}{\partial z} - \frac{3}{4}\frac{C_\mathrm{D}}{d}\alpha_\mathrm{G}\alpha_\mathrm{L}\rho_\mathrm{L}\left|\vec{v}-\vec{u}\right|\Big\langle V_z - U_z\Big\rangle \tag{4.30}$$

The dependence on α_G cancels across all terms. The difference between the mean velocities, averaged at the position of the particle, is the slip velocity U_0. If it is also substituted as the characteristic magnitude of $\left|\vec{v}-\vec{u}\right|$, it follows that

$$\boxed{\left|U_0\right|U_0 = \frac{4}{3}\frac{d}{C_\mathrm{D}\alpha_\mathrm{L}\rho_\mathrm{L}}\left(-\frac{\partial P}{\partial z} - \rho_\mathrm{G} g\right)} \tag{4.31}$$

This expression has a radial dependence for swirling flows due to the non-homogeneous distribution of the liquid phase $\alpha_\mathrm{L}(r)$, which needs to be calculated in tandem. When decay of the swirling motion is taken into account, as illustrated in section 3.4, radial variations in the pressure gradient lead to additional variation of U_0 with r.

For calculating the drag coefficient, the Schiller-Naumann correlation is used [19]. This expression was derived for solid particles in a fluid, but is often deemed appropriate for gas bubbles of relatively small size that are predominantly forced by liquid motion:[4]

$$C_\mathrm{D} = \begin{cases} \dfrac{24}{\mathrm{Re}_p}\left(1 + \mathrm{Re}_p^{0.687}\right) & \mathrm{Re}_p \le 1000 \\ 0.44 & \mathrm{Re}_p > 1000 \end{cases} \tag{4.32}$$

Note that U_0 is used to define Re_p and therefore equation (4.31) requires iterative solving.

---

[3] The swirl number Ω is ill-defined for use in multiphase flows [9]. However, because this thesis considers a mixture flow with low gas content, it is reasoned that in this limit Ω remains of relevance when only the liquid phase velocities U_z and j_L are used. These are substituted in equation (4.29).

[4] It is repeated here that the particular correlation used is not essential to the modelling framework, and others can be used if more appropriate. See, for instance, [23].

4.2.2 Radial distribution of volumetric fractions

Prior to solving for the volumetric fractions, an expression is required for the radial pressure gradient that occurs due to the swirling motion. This is the predominant force mechanism responsible for the non-homogeneous distribution of phases. Its magnitude can be deduced from the r-momentum equation for the mixture, avoiding the need to consider interfacial momentum transfer.[5]

Reynolds has estimated that in (4.24), the relative magnitude of liquid turbulent stresses is only $\mathcal{O}(1\%)$ [18]. In the low gas limit, a similar scaling is expected for turbulent stresses of the gas phase. If both these contributions are neglected, it follows that

$$\frac{\partial P}{\partial r} \;=\; \big(\alpha_{\mathrm{G}}\rho_{\mathrm{G}} + \alpha_{\mathrm{L}}\rho_{\mathrm{L}}\big)\,\frac{U_\theta^2}{r} \tag{4.33}$$

The distribution of the volumetric gas fraction can now be obtained from the r-momentum equation for the gas phase. The liquid distribution follows automatically, since

$$\alpha_{\mathrm{L}}(r) \;=\; 1 - \alpha_{\mathrm{G}}(r) \tag{4.34}$$

In the balance equation for the gas phase, interfacial momentum transfer consists of two contributions: turbulent dispersion (4.19) and lift (4.23). There is no substantial drag because the mean radial velocities are negligible. The tangential velocity of both phases is represented as U_θ. Substituting for the radial pressure gradient, and rearranging terms in U_θ^2/r, the resulting balance equation can be written as:

$$0 \;=\; -\alpha_{\mathrm{G}}\alpha_{\mathrm{L}}\big(\rho_{\mathrm{L}} - \rho_{\mathrm{G}}\big)\frac{U_\theta^2}{r} - \frac{3}{4}\frac{C_{\mathrm{D}}}{d}\rho_{\mathrm{L}}\big|\vec{v}-\vec{u}\big|\mathbb{D}_t\frac{\partial \alpha_{\mathrm{G}}}{\partial r} - \alpha_{\mathrm{G}}\alpha_{\mathrm{L}}\rho_{\mathrm{L}}C_{\mathrm{L}}\big|\vec{v}-\vec{u}\big|\frac{\partial U_z}{\partial r} \tag{4.35}$$

A constant lift coefficient C_{L} is used, which is determined by bubble size. U_0 is substituted for the relative velocity scale $\big|\vec{v}-\vec{u}\big|$ from (4.31). The resultant expression can be solved for $\alpha_{\mathrm{G}}(r)$ by separation of variables and subsequent integration:

$$\int \frac{\mathrm{d}\alpha_{\mathrm{G}}}{\alpha_{\mathrm{G}}\big(1-\alpha_{\mathrm{G}}\big)} \;=\; -\int \left\{\frac{4}{3C_{\mathrm{D}}}\frac{d}{\mathbb{D}_t}\left(\frac{\rho_{\mathrm{L}}-\rho_{\mathrm{G}}}{\rho_{\mathrm{L}}}\frac{1}{\big|U_0\big|}\frac{U_\theta^2}{r} + C_{\mathrm{L}}\frac{\partial U_z}{\partial r}\right)\right\}\mathrm{d}r \tag{4.36}$$

The left hand side integral has an analytical solution. The right hand side depends on the input conditions and the current values of parameters that are simultaneously solved for. It is convenient to express this as:

$$-\ln\left|\frac{1-\alpha_{\mathrm{G}}}{\alpha_{\mathrm{G}}}\right| \;=\; -f(r) + K \tag{4.37}$$

The constant K is fixed per iteration by the integral limit condition (4.27) for given j_{G}. An explicit expression for $\alpha_{\mathrm{G}}(r)$ follows by exponentiating and rearraging terms:

$$\boxed{\begin{aligned} \alpha_{\mathrm{G}}(r) \;&=\; \frac{K}{K + \exp\big(f(r)\big)} \\ \text{where}\quad f(r) \;&=\; \int_0^r \left\{\frac{4}{3C_{\mathrm{D}}}\frac{d}{\mathbb{D}_t}\left(\frac{\rho_{\mathrm{L}}-\rho_{\mathrm{G}}}{\rho_{\mathrm{L}}}\frac{1}{\big|U_0\big|}\frac{U_\theta^2}{r'} + C_{\mathrm{L}}\frac{\partial U_z}{\partial r'}\right)\right\}\mathrm{d}r' \end{aligned}} \tag{4.38}$$

---

[5] It is possible to use the mixture conservation equation even with slip in the z-direction, as (U_z, V_z) only occur in combination with $\partial/\partial z(...)$, which is assumed to be negligible cf. section 4.1.1.

4.2.3 Streamwise velocity profiles

To estimate the streamwise velocity profiles, the z-momentum equation for the liquid phase is considered. In this case, turbulent stresses compensate the applied pressure gradient for up to 90 percent, as estimated by Reynolds [18]. U_z does not occur directly in (4.26), but it is solved for via the turbulent stresses by using the Boussinesq closure hypothesis. However, the non-homogeneous distribution of both phases complicates this approach. In local flow regions of reduced α_{L}, the one-way coupling assumption $\langle \mathcal{F}_{\mathrm{L}z} \rangle \sim 0$ fails and solving the liquid momentum equation becomes increasingly difficult.

To account for the correct limit behaviour, the mixture z-momentum equation is used instead, with the inclusion of both liquid and gas turbulent stresses. In regions of low α_{L}, the pressure gradient then simply drives the gas stresses. This approach avoids interfacial momentum transfer and possible coupling issues altogether. In analogy to the solution strategy for single-phase turbulent flow, the mixture equation is integrated over the cross section to solve for the total stress $\tau_{zr}(r)$:

$$0 \;=\; -\iint \big(\underbrace{\alpha_{\mathrm{G}}\rho_{\mathrm{G}} + \alpha_{\mathrm{L}}\rho_{\mathrm{L}}}_{\rho(r)}\big)\, g\, r\, \mathrm{d}r\, \mathrm{d}\theta \;-\; \iint \frac{\partial P}{\partial z}\, r\, \mathrm{d}r\, \mathrm{d}\theta \;+\; \iint \frac{1}{r}\frac{\partial}{\partial r}\Big(r\,\tau_{zr}\Big)\, r\, \mathrm{d}r\, \mathrm{d}\theta \qquad (4.39)$$

It is assumed that the velocity fluctuations of the gas phase are caused by the liquid turbulent stresses, and therefore $\overline{v_i' v_j'} \sim \overline{u_i' u_j'}$. This is common practice for bubbly flows, where the constant of proportionality between fluctuating quantities of each phase is nearly 1 [11]. In the case of absolute equality, the total stress in the core flow region is expressed as:

$$\tau_{zr}(r) \;=\; -\Big(\underbrace{\alpha_{\mathrm{G}}\rho_{\mathrm{G}} + \alpha_{\mathrm{L}}\rho_{\mathrm{L}}}_{\rho(r)}\Big)\, \overline{u_z' u_r'} \qquad (4.40)$$

If $\overline{u_z' u_r'}$ is related to the mean velocity gradient by the Boussinesq hypothesis, and the eddy viscosity is estimated by (4.8), the above expressions for τ_{zr} can be combined to:

$$\boxed{\rho(r)\, L^2 \left|\frac{\partial U_z}{\partial r}\right| \frac{\partial U_z}{\partial r} \;=\; \frac{1}{r}\int_0^r \Big(-\frac{\partial P}{\partial z} - \rho(r')g\Big)\, r'\, \mathrm{d}r'} \qquad (4.41)$$

This relation can be solved for $U_z(r)$ up to an integration constant. To find it, the observation that the law of the wall holds in swirling flows is used: the velocity profile is required to match the logarithmic solution at the outer edge of the core region. From section 4.1.2, this boundary is at $r = 0.43\,D$ (or equivalently, $y = 0.07D$) and therefore

$$U_z\big(0.43\,D\big) \;=\; u_*\left(\frac{1}{k}\ln\!\Big(0.07\,\frac{u_* D}{\nu}\Big) + 5.0\right) \qquad (4.42)$$

Note that, because a gas-liquid flow is considered, the friction velocity u_* (equation (4.10)) is defined using the mixture density $\widetilde{\rho}$.

4.2.4 Influence of swirl decay

Up to here, the input parameters required for solving equations (4.31), (4.38) and (4.41) have been considered to be independent from one another. In reality, the axial pressure gradient and U_θ are linked. Experiments indicate that the pressure gradient varies with radial position due to swirl decay, as discussed in section 3.4. However, these effects are neglected under the quasi-1D assumption that streamwise derivatives have a negligible influence on the dynamics of the cross-section (section 4.1.1: 5). It is insightful to investigate the validity of this assumption in more detail.

An expression for the axial pressure gradient can be obtained by integrating (4.33) with respect to r, and differentiating with respect to z:

$$\frac{\partial P}{\partial z}(r) \;=\; \frac{\partial P_0}{\partial z} \;-\; \frac{\partial}{\partial z}\int_r^R \rho(r)\,\frac{U_\theta^2}{r}\,\mathrm{d}r \tag{4.43}$$

Here P_0 is the pressure at the wall, where $U_\theta = 0$ (no-slip condition). This expression illustrates clearly the scaling issue that occurs: the wall pressure gradient is approximately hydrostatic ($\rho_\mathrm{L} g$), but the centripetal accelleration $U_\theta^2/r \gg g$. (This is exactly why swirl separation is faster than gravitational settling, but here it poses a modelling issue.)

If there is no swirl decay, the rightmost term in (4.43) is exactly zero. However, if streamwise variations are small but nonzero, the large magnitude of U_θ^2/r implies that there might still be significant influence on the axial pressure gradient. If so, the quasi-1D approach fails and cross-sectional balance equations cannot be accurately solved without knowledge of the swirl decay. To deduce a condition on the applicability of the quasi-1D approach, the derivative can be expanded inside the integral to write:

$$2\,\rho_\mathrm{L}\int \frac{\partial U_\theta}{\partial z}\,\frac{U_\theta}{r}\,\mathrm{d}r \;\ll\; \rho_\mathrm{L} g \tag{4.44}$$

This is a much more stringent condition than that of relatively small streamwise derivatives. For the left-hand expression to be negligible compared to the wall pressure gradient, a flow problem must have either low swirl magnitude, very slow decay with downstream distance, or a combination of both at any given point. Using characteristic scales $U_\theta/\mathcal{U}$, r/D and z/ℓ to normalize the integral to $\mathcal{O}(1)$ yields a Froude number criterion for the applicability of the quasi-1D approach:

$$\mathrm{Fr}^2 \;=\; \frac{\mathcal{U}^2}{g\ell} \ll 1 \tag{4.45}$$

A simple model extension to incorporate swirl decay

In cases of $\mathrm{Fr} \geq 1$, the decay of U_θ with downstream distance will influence the model output. If however, it can be assumed that all other streamwise variations remain negligible, the solving routine can be extended using a simple decay model. For single-phase swirling flow, multiple authors have reported exponential decay of the swirl number Ω [15, 30]. In relation to the above, this implies that U_θ can be expressed as:

$$U_\theta(r,z) \;=\; U_\theta(r)\,e^{-\xi(z/D)} \tag{4.46}$$

Here ξ is a decay parameter, which in general depends on the Reynolds number and local swirl intensity of the flow. Experiments indicate it is of order $\mathcal{O}(10^{-2})$. Specifying ξ allows for extending the solving routine by (4.43) and (4.46) to incorporate effects of swirl decay:

$$\text{input}\quad \left(\frac{\partial P_0}{\partial z},\, j_\mathrm{G},\, U_\theta,\, \xi\right) \;\longrightarrow\; \left(\frac{\partial P}{\partial z},\, U_0,\, U_z,\, \alpha_\mathrm{G},\, \alpha_\mathrm{L}\right) \quad \text{output}$$

In the next chapter, results obtained using the quasi-1D approach and this simple swirl decay model are comparatively analysed.

4.2.5 Solver loop

The parameters (U_0, U_z, α_{G}, α_{L}) can be obtained for given input conditions by simultaneous solving of equations (4.31), (4.38) and (4.41). Because of the interdependence of these parameters, solving is best performed numerically with an iterative procedure. The next chapter illustrates several cases using an implementation in MATLAB. The corresponding solver code can be referenced in Appendix B. In this section, specific steps are further illustrated for the sake of understanding.

- *Initiate variables:* in addition to the fixed input and material parameters, the iterative solver requires initial assumptions on the quantities to be calculated. The following simple, constant estimates are used:

  U_0 : 0.25 m/s α_{G} : 0.01
  U_z : plug flow, based on input α_{L} : 0.99

  The velocity gradient required to calculate ν_t is approximated by a constant U_z/D.

- *Redefine variables:* after each iteration, the calculated quantities can be used to refine dependent variables. Here, the eddy viscosity is estimated using a correlation by Sato:

  $$\nu_t(r) \;=\; L^2 \left|\frac{\partial U_z}{\partial r}\right| + 0.6\, d\, \alpha_{\mathrm{G}} \left|U_0\right| \tag{4.47}$$

  This correlation has two contributions. The first accounts for the effects of the liquid velocity gradient (shear) on the turbulence intensity, and is equal to the mixing length definition (4.8). The second accounts for *bubble-induced* turbulence, which occurs when the wake dynamics of a bubble rising through the liquid influence the trajectories of adjacent bubbles. This effect scales with bubble diameter, concentration (α_{G}) and slip velocity. A key assumption in the correlation is that both mechanisms are weakly coupled so that they can be superposed linearly [12, 10].

  Because of the non-homogeneous gas distribution in swirling flow, the effect of bubble-induced turbulence is expected to strongly affect ν_t near the centerline. This also avoids a classical difficulty in mixing length theory, where the velocity gradient equals zero at the centerline by symmetry, but the eddy viscosity should not [11].

  Redefinition of ν_t also implies that the effects of turbulent dispersion become position-dependent on the next iteration, i.e. $\mathbb{D}_t = \mathbb{D}_t(r)$. Additionally, it is possible after each iteration to correct the slip velocity U_0 by incorporating an estimate for the turbulent gas stresses neglected in (4.31), but this was not pursued further.

- *Convergence:* a convergence criterion may be formulated for any (combination) of the calculated quantities, often in the form of limited percentual change compared to the previous iteration, e.g. <1%. In this thesis the solver loop was repeated until all quantities stopped varying, which generally takes between 5–30 iterations. However, a convergent solution does not exist for all combinations of input parameters.

Chapter 5

Modelling results

This chapter features a range of possible outputs that can be obtained using the modelling framework developed, for a swirling air-water flow in a vertical pipe. The use of air and water as constituent phases allows for experimental verification of these results with the TOMOCON setup. This is the focus of chapters 6 and 7.

Fixed parameters

With the exception of the input conditions to the solver, all physical parameters are constant throughout the different cases illustrated below. The values used can be referenced in table 5.1. The input flow has a uniform bubble size distribution of 2.5 mm. From visual observations of homogeneous bubbly flow in the TOMOCON setup, this appears to be a suitable estimate.

The inner pipe diameter D is taken equal to that of the setup. The mixing length in the core of the flow is approximated by $L = \beta R$, as in section 4.1.2. For pipe flow, experiments have indicated that $\beta \approx 0.13$ [27].

The lift coefficient is obtained using the Tomiyama lift correlation, which involves various expressions for C_L dependent on bubble shape, that are quantified through the Eötvös number [21].

d	2.5	mm
D	81.4	mm
ρ_G	1.2	kg/m^3
ρ_L	1000	kg/m^3
ν_G	$1.5 \cdot 10^{-5}$	m^2/s
ν_L	$1.0 \cdot 10^{-6}$	m^2/s
L	$5.3 \cdot 10^{-3}$	m
g	9.81	m/s^2
k	0.4	[–]
C_L	0.3	[–]

Table 5.1: Fixed parameters

Input conditions

Previous work on an axial hydrocyclone similar to the TOMOCON setup has shown that the tangential velocity profile resembles a Gaussian vortex [32, 31]. This profile is characterized by a smooth transition between a forced vortex inner region and a free vortex outer region:

$$U_\theta(r) \;=\; \frac{B}{r}\left(1 - e^{-\gamma(r/R_c)^2}\right) \tag{5.1}$$

The boundary between these regions is determined by the core radius R_c. Here, the velocity profile has its maximum. The parameter B reflects the magnitude of the vortex, and the exponential falloff is determined by the constant $\gamma = 1.256$.

Numerical simulations indicate that R_c/D is in the range 0.1–0.2 for the TOMOCON setup [33]. In the following sections, equation (5.1) is used as input with $R_c = 0.2$ in all cases. Different swirl intensities are obtained by various input values for B. Several tangential velocity profiles that result are depicted in figure 5.1a.

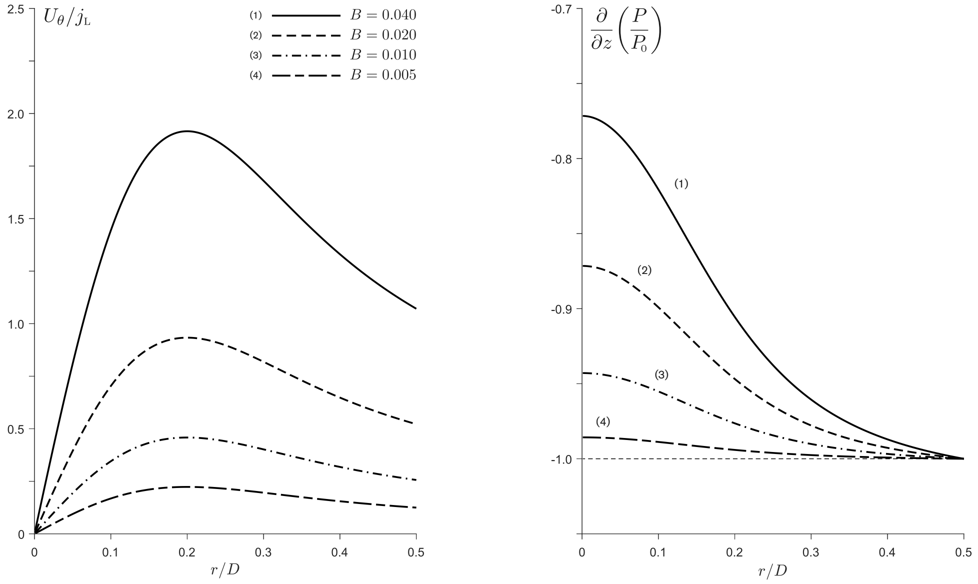

(a) tangential velocity profile

(b) axial pressure gradient

Figure 5.1: Various magnitudes of $U_\theta(r)$ based on (5.1) and axial pressure gradients used as input conditions for the quasi-1D and swirl decay models.

$$\frac{\partial P}{\partial z} = 1.005\,\rho_\mathrm{L} g \qquad j_\mathrm{G} = 0.01 \text{ m/s}.$$

The axial wall pressure gradient takes on values slightly above hydrostatic equilibrium, in order to ensure a net upflow for any given fluid mixture. Because the input flow is bubbly, the superficial gas velocity j_G is roughly in the range 0–0.1 m/s. In the swirl decay model, a constant $\xi = 0.02$ is assumed. For a range of U_θ, its effect on the radial variation of the axial pressure gradient is illustrated in figure 5.1b.

5.1 Radial distribution of the gas fraction

Dependence on U_θ

The tangential velocity is the source of the centripetal forces responsible for swirl separation. From figure 5.2a it follows that these have a pronounced effect on the distribution of $\alpha_\mathrm{G}(r)$. Here, the tangential velocity profiles $U_\theta(r)$ from figure 5.1a have been used in solving equation (4.38). As a result, the gas fraction peaks near the centerline, with near-zero concentrations for the remainder of the cross section, even for relatively low rotation rates.

It seems the inward-oriented forces in (4.35) dominate the dynamics of the cross section. Large gradients in the gas distribution are required for turbulent dispersion to balance the radial pressure gradient. At fixed j_G, this implies the bulk of the cross section is void of bubbles. The lift force is directed outward (but with negligible magnitude in the core flow) for the quasi-1D model, and inward for the swirl decay model, further increasing separation.

The distributions of $\alpha_\mathrm{G}(r)$ can locally peak above the transition threshold for bubble coalescence derived for gas-liquid flow without swirl (equation (3.1)), even though the cross-sectional average $\widetilde{\alpha}_\mathrm{G}$ remains well below. This behaviour is expected to yield a transition from bubbly to columnar flow. The next section further elaborates on this transition.

The same trend is observed for the quasi-1D and swirl decay models, but exact results differ because of the radial distribution of the pressure gradient cf. figure 5.1b. This affects force mechanisms that scale with U_0, U_z or its derivatives. Notable changes occur in the eddy viscosity ν_t, the lift force orientation, and the integral condition (4.27) on j_{G} that is used to normalize the gas distribution.

Dependence on j_{G}

Figure 5.2b illustrates the effect of increasing superficial gas velocity on $\alpha_{\mathrm{G}}(r)$. An increased flow rate of gas implies higher gas content in every cross section, but its distribution is not straightforward: the additional gas does not all add up near the centerline.

Rather, the increased gas content leads to a higher mixture velocity if the input pressure gradient remains equal, because of the reduction in weight that results. This is reflected in an increased higher superficial liquid velocity j_{L}, which lowers the swirl number Ω for given U_θ according to equation (4.29). A lower swirl intensity yields a less distinct separation of phases. Therefore, it is observed that the gas distribution extends outward as well as upward, rather than peak at the center.

5.1.1 A qualitative transition criterion

There is no physical basis to expect the threshold condition for increased bubble coalescence ($\alpha_{\mathrm{G}} = 0.25$) to differ between flows with and without swirl. It is therefore proposed to retain this criterion for swirling gas-liquid flow, but in the context of transition from bubbly to columnar flows. Under the influence of swirling motion, coalescence does not lead to the formation of wide, bullet shaped bubbles associated with slug flow, but rather to the formation of a columnar flow of distinct (fully separated) gas and liquid phases.

However, it appears improbable that crossing this threshold at a certain radial position immediately results in transition from a bubbly to a columnar flow pattern. Instead, it is expected that instabilities will start to occur over a range of input conditions that yield $\alpha_{\mathrm{G}}(r)$ near 0.25 locally. Full transition is likely whenever a significant fraction of the total bubble concentration is located in flow regions of $\alpha_{\mathrm{G}} \gtrsim 0.25$.

Using the modelling output, this reasoning can be related to the fractional area under the gas distribution profile that lies above the 0.25 threshold. If an engineering assumption is made on when this fractional area is significant, say from 10 percent, a qualitative criterion for transition from bubbly to columnar flows could be:

$$\int_0^x \Big(\alpha_{\mathrm{G}}(r) - 0.25\Big)\, r\, \mathrm{d}r \Big/ \int_0^R \alpha_{\mathrm{G}}(r)\, r\, \mathrm{d}r \ \sim\ 0.1 \tag{5.2}$$

Here, x is the radial position at which the gas distribution profile intersects the 0.25 threshold. This approach is illustrated for two cases in figure 5.3.

Further research could provide a better estimate for the impromptu 10 percent threshold used here for the purpose of illustration. However, a more suitable approach towards a *quantitative* transition criterion is to employ a collision model for studying the physical mechanisms associated with coalescence. This would also allow for the transition criterion to be generalized to other constituents than air and water. The effects of surface tension are believed to play an important role here, as it is a key parameter in non-dimensional numbers associated with disperse flow (We, Eö) and in the transition criteria developed for non-swirling flow discussed in chapter 3 [24]. This was not investigated as part of this thesis, but is a recommended trajectory for further research. .

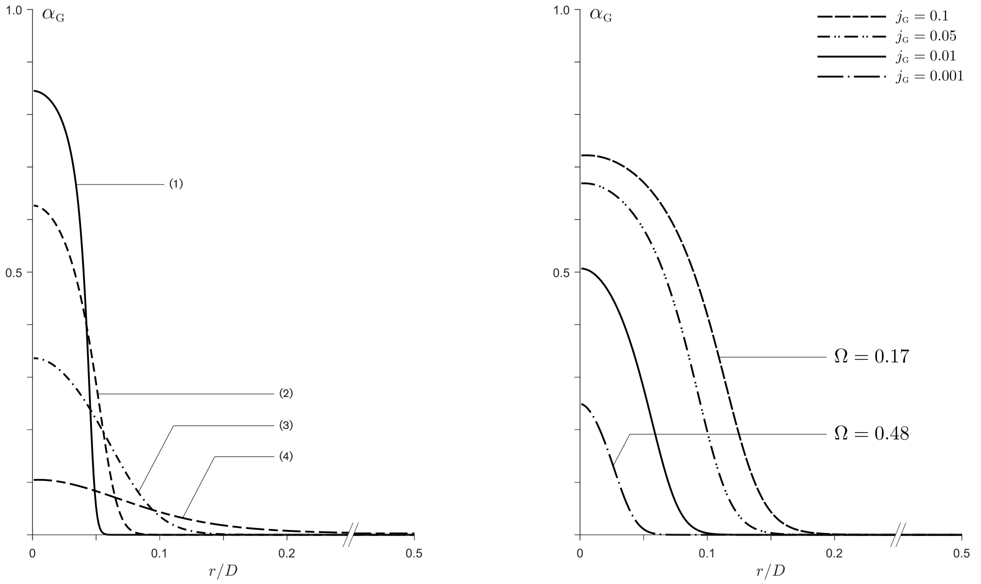

(a) dependence on U_θ

(b) dependence on j_G

Figure 5.2: Radial dependence of gas fraction $\alpha_G(r)$ for the quasi-1D model.

$$\frac{\partial P}{\partial z} = 1.005\,\rho_L g \qquad j_G = 0.01 \text{ m/s (a)} \qquad B = 0.015 \text{ m/s (b)}$$

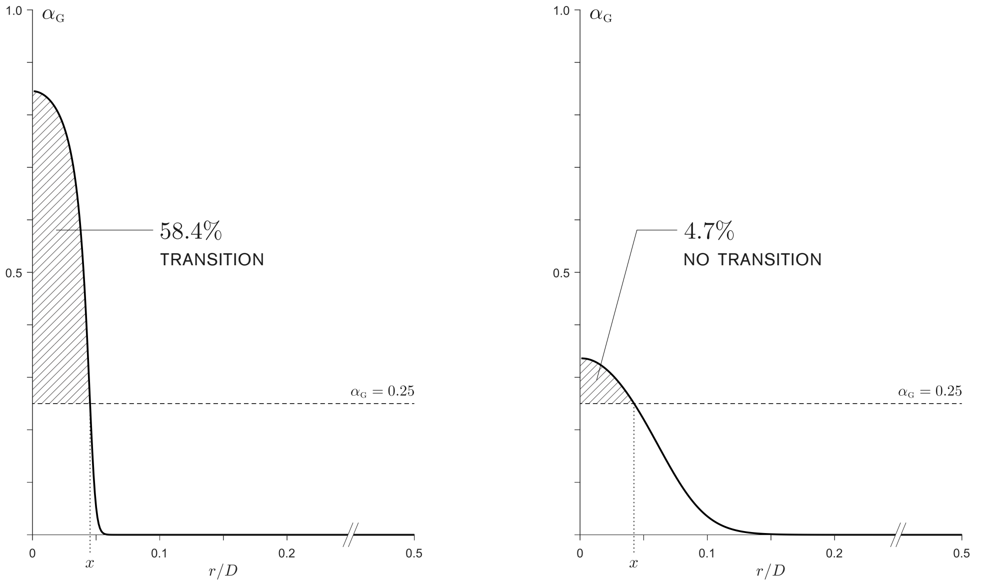

(a) $B = 0.04$ m/s

(b) $B = 0.01$ m/s

Figure 5.3: A qualitative transition criterion for the onset of columnar flow, based on graph area above the coalescence threshold.

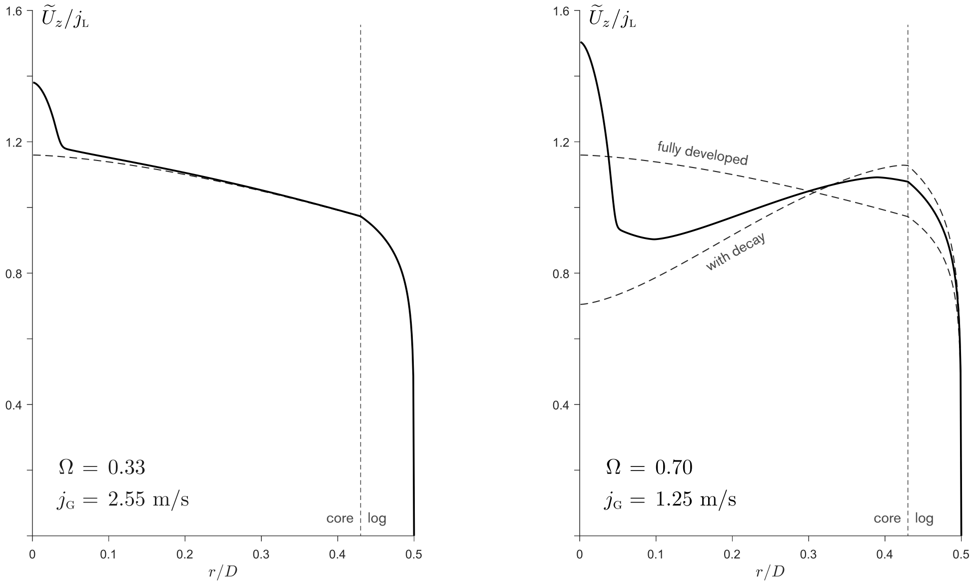

(a) quasi-1D

(b) with swirl decay

Figure 5.4: Streamwise mixture velocity profiles $\widetilde{U}_z(r)$ obtained from the different models. There are significant differences in trend and magnitude of related quantities j_L, Ω. Single-phase velocity profiles (dashed lines) are superposed for reference.

5.2 Streamwise velocity profiles

The quasi-1D and swirl decay models can lead to significantly different axial velocity profiles as the magnitude of U_θ increases. Apart from a difference in trend, the magnitude of related quantities (j_L, Ω) is strongly affected. Figure 5.4 provides an illustration for a case of substantial tangential velocity. To benefit understanding of how the phase distribution affects the velocities, these graphs make use of the mixture velocity, which is defined as:

$$\widetilde{U}_z(r) \ = \ \alpha_G \big(U_z + U_0\big) + \alpha_L U_z \tag{5.3}$$

In the quasi-1D model, the axial pressure gradient is constant. As a result, the mixture velocity has a strong resemblance to a fully developed turbulence profile, but with a peak of higher velocity in regions of increased gas content. This is in contrast to experimental observations, which often mention a near-stagnation of liquid flow when approaching the centerline [7]. Such behaviour can also be observed in the TOMOCON setup.

It is assumed that in these cases, the conditions of swirl are such that characteristic flow scales yield Fr ≥ 1 in (4.45). It thus appears that for practical separation conditions, the inclusion of swirl decay effects is required to accurately predict phase and velocity distributions. A quasi-1D approach to swirling flow is only applicable far downstream of the swirl origin, where the flow has nearly recovered to a fully developed state.

The velocity profile obtained using the swirl decay model (figure 5.4b) is in better agreement to observations. The radial variation of the pressure gradient leads to a negative inclination in liquid velocity when moving inward from the edge of the log-layer, where boundary condition (4.42) is enforced. However, note that the mixture velocity peaks more strongly where the gas is located in comparison to figure 5.4a.

Local reduction of the pressure gradient has a much stronger effect on the liquid than on the gas due to its weight. The next section elaborates on this for single-phase flow.

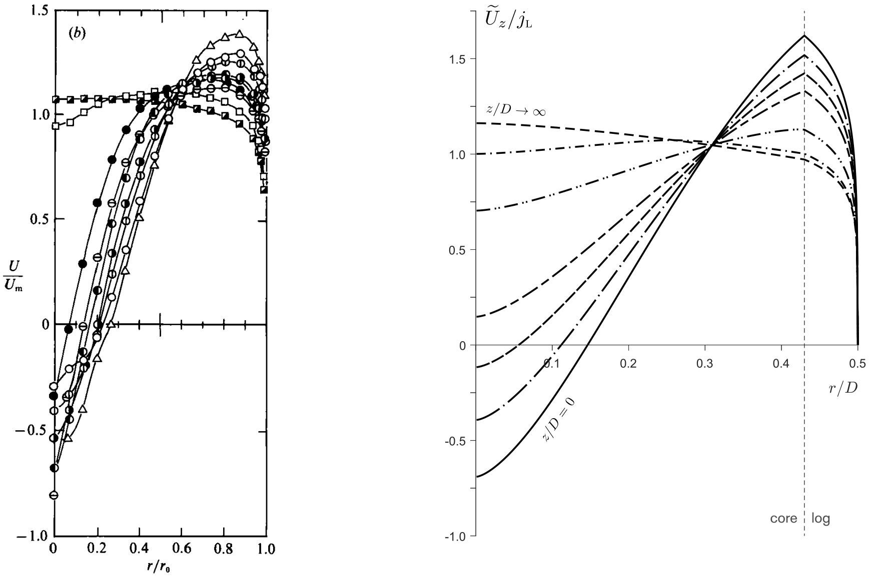

(a) measurement data

(b) modelling output

Figure 5.5: Comparison of streamwise velocity profiles $U_z(r)$ for single-phase flow, influenced by swirl decay. Measurement data in figure (a) from [15].

5.2.1 Comparison to single-phase measurements

The effect of swirl decay on the streamwise velocity profile is more intuitively understood for single-phase flow. Also, there is measurement data available in the literature for comparison. Figure 5.5 relates output velocity profiles from the swirl decay model (water only) to results obtained by Kitoh, using hot-wire anemometry of a swirling air flow at various locations along a horizontal pipe [15]. These graphs show very similar behaviour. This is an indicator that the modelling framework with swirl decay covers all relevant physical mechanisms.

In both sequences, the velocity profile has a characteristic V-shaped form: towards the centerline, the local pressure gradient (4.43) provides less upward force and the fluid moves at low velocity, if at all. Regions of net adverse pressure gradient can even occur, in which the fluid is accelerated in the upstream direction, causing backflow. These effects are reduced with downstream distance, as local values of U_θ and its rate of decay drop and the velocity profile flattens out. In the near-wall region, flow is upward in all cases. This is reflected in its characteristic scale: the friction velocity u_* by definition (4.10) relates to the *average* pressure gradient across the pipe, which is still in the favourable direction.

From figure 5.4b, it appears backflow is less likely to occur in gas-liquid flows due to the gas peak velocity near the centerline. However, immediate stalling results whenever instabilities break a columnar flow and liquid bridges the pipe. This leads to gas bursts originating upstream and other complicated dynamics often observed in practice.

5.3 Discussion

Convergence

The solving routine described in section 4.2 does not always lead to a convergent solution. In cases where the input U_θ is high with respect to the calculated streamwise velocity, the centripetal forces in equation (4.35) are so strong in comparison to the effects of dispersion and lift that full separation occurs. The gas distribution approaches a step function, with a region of $\alpha_{\mathrm{G}} = 1$ near the centerline and a near-vertical falloff to zero for the remainder of the cross section. The distribution of liquid shows the inverse behaviour.

This generates large peaks in the velocity profile in the central region, which on the next iteration reduce α_{G} to a near-homogeneous distribution. This subsequently dampens the strong variations in U_z. Both profiles alternate between their limit states antagonistically with further iteration, never approaching a convergent state. Such behaviour occurs in both the quasi-1D model and the swirl decay model.

These observations are indicative of the limits of a disperse flow model. The complete absence of liquid in local flow regions invalidates the use of a slip velocity concept, and its use as a representative scale for the effects of drag and lift in (4.35). Here, the modelling framework as developed in chapter 4 breaks down. However, the transition from a bubbly to a columnar flow pattern will have occurred long before. We therefore have to conclude that in this limit, the flow will be columnar and that it is not possible to quantify it from a disperse flow approach. An interesting objective for further research would be to develop a separated flow model for columnar flows and study the transition to bubbly flow in the reverse direction, i.e. when separated flow can no longer be sustained.

It is important to stress here that such a model will strongly differ from a regular annular flow approach. In the latter, the pressure gradient is not high enough to balance the weight of the liquid film, but the high-velocity gas core drags it upward. In the case of (low gas content) columnar flows, pressure gradients are near or above hydrostatic, the liquid phase dominates the physics, and the gas follows suit. This implies a different take on solving the governing equations.

Need for experimental verification

From extensive testing of the solving routine for various input conditions, it appears that its applicability is limited to swirl intensities $\Omega \lesssim 1$. Above this threshold, the model predicts full separation near the centerline, and a columnar flow pattern will have formed.

The axial cyclones used in the TOMOCON setup incur a fixed swirl intensity to any input flow in the range $\Omega = 1.7$–6.7 [31]. Therefore it is not possible to correlate the modelling output to the flow maps developed for the setup in previous research [34]. Based on the model behaviour, it is predicted that for any homogeneous bubbly input flow, a columnar flow will result when applying these swirl intensities. However, the flow maps developed consistently show a threshold on j_{L} that needs to be surpassed in order to yield columnar flow patterns. This discrepancy requires further experimental investigation, to be able to conclude whether the modelling framework is flawed or previous observations are off in the limit of low gas flow rate. Another explanation might be that the swirl number does not allow for easy generalization to multiphase flows as in (4.29), and its definition may have to be altered. Two objectives were considered for experimental verification:

(i) To extend and/or partially revisit the flow maps developed for the TOMOCON setup, for values of j_{G} representative of homogeneous bubbly flow in the low gas limit.

(ii) To obtain a proper estimate of $U_\theta(r)$ for the operating conditions and geometry of the setup, as this is essential for a correct prediction of the distribution of phases over the cross section. This also allows for bypassing the swirl number Ω as a measure of swirl intensity when characterizing multiphase flows.

The next chapter describes in further detail the experimental methods employed to pursue the above objectives.

PART 3

Experiments

Chapter 6

Experimental approach

This chapter describes the approach to experimental verification of the modelling output using the TOMOCON setup. Throughout this thesis, it is operated without any output control to avoid possible influences of actuation on the dynamics of the swirling flow. This means separation efficiency is generally low, but the physical mechanisms involved can be studied on a fundamental level.

To extend previous flow maps towards lower gas flow rates, the setup is fitted with an accurate low-range air flow controller. Other experimental conditions are equal to those used by Ammerlaan [34]. This is detailed in section 6.1. Estimates of the tangential velocity U_θ are obtained via intrusive differential pressure measurements, using equation (4.33) as a pressure-velocity correlation. This is the subject of sections 6.2–6.3.

6.1 Setup

Flow loop

The experimental setup for the TOMOCON research at TU Delft's Transport Phenomena group is a pressure-driven flow loop for separation of air and water, built around a series of interchangeble axial cyclones of different swirl intensity. It is equipped with a wide range of sensing and actuation components for control, that can be set and monitored with a LABVIEW software routine. Figure 6.1 provides a schematic illustration.

At its core is a vertical pipe section of circa 5 meters, of which roughly half (2.74 m, $33.6\,D$) is used as development length for the input flow before entering the cyclone. After, there is a separation section of 1.3 m where the flow can be monitored before it is collected in separate, concentric outlets. The majority of pipe sections is in clear PVC to allow for flow observation. The cyclone elements are opaque. The central light phase outlet has an inner diameter of 50 mm (DN50), for the outer pipe (DN80) an inner diameter of 81.4 mm has been used in constructing the previous flow maps. This value is consequently used here to enable a comparison to these measurements.

Water is supplied from a 1000 L buffer vessel by either of two centrifugal pumps installed in parallel, depending on the flow rates required. In this thesis, only the smaller pump was used (Iwaki MX402CV5E, nominal 200 L/min, 2 barg). Air is injected through a purpose-built sparger that is locally inserted in the flow, consisting of 4 closed-end metal tubes fitted with a string of perforations. The air flow stems from the building's compressed air system and is controlled by a Bronkhorst 'El-Flow Select' Mass Flow Controller. For research at low gas flow rates, this thesis required a different controller from the one used under normal operating conditions, and which was used by Ammerlaan. This adjustment is further elaborated on below.

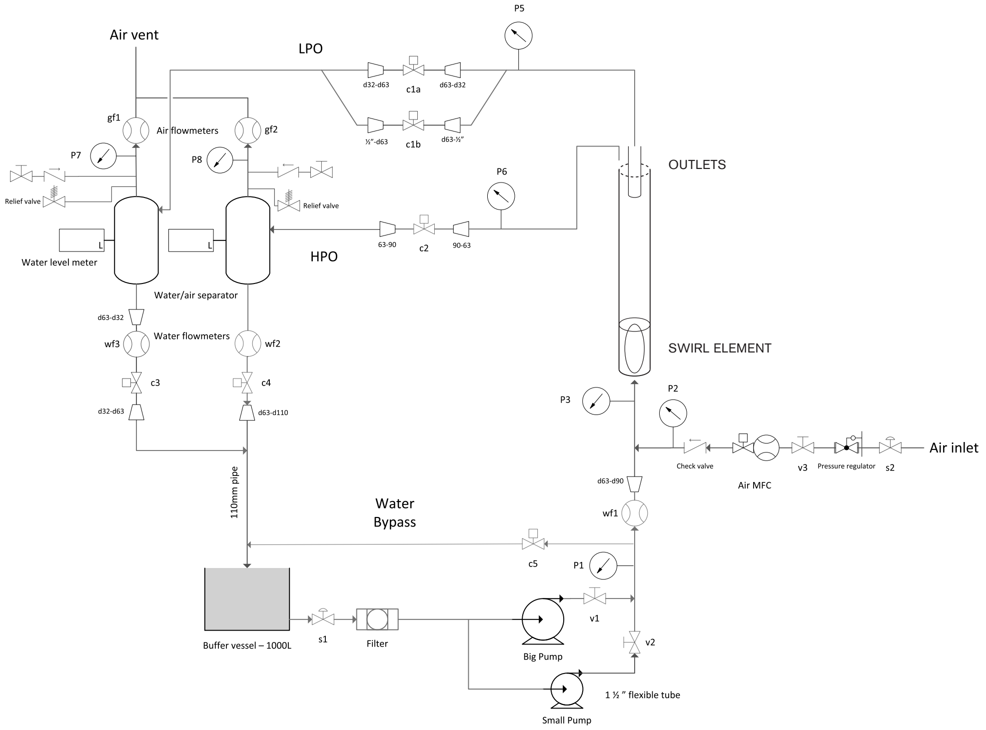

Figure 6.1: Schematic overview of the TOMOCON setup

A wall pressure sensor (GE UNIK 5000 gauge, p_3) installed just prior to the separation section accounts for corrections to the flow rates predicted by the pump and air flow controller settings. This was not installed at the time of Ammerlaan's research, and should yield increased measurement accuracy.[1] After the separation section, both outlets lead to settling tanks from which air is vented out at the top, into the building's exhaust ventilation system. The water is recirculated to the buffer vessel below. Flow rates on all these streams are monitored for control purposes, and can be enforced by various valves.

The above is a reduced description of the setup, applicable to research without control. An in-depth treatment of all its aspects is covered in the setup manual [35]. It can be obtained through the Transport Phenomena secretariat.

Cyclone geometry

A series of 4 axial cyclone geometries ('swirl elements') is used with the TOMOCON setup. These are rigid, streamlined bodies equipped with helical vanes, of which the exit angle ϑ determines the intensity of swirl. Figure 6.2 shows elements 1 and 3, which were used in this thesis, with their respective angles and swirl intensities. These elements were 3d-printed in DN100 encasings as part of the PhD research of Van Campen [31].

When a mixture flow is forced along a swirl element, part of the input linear momentum is converted into swirling motion (angular momentum). Ammerlaan's thesis focused on understanding the swirl element as a transfer function between upstream and downstream conditions, governed by complex dynamics inside. For the abstract modelling perspective employed in this thesis, such understanding is less relevant. Rather, swirl elements 1 and 3 were chosen for use in the experiments on different grounds.

---

[1] In his thesis, Ammerlaan uses pressure data from sensor p_1 installed directly behind the pumps (i.e. water flow only) and employs a constant -0.07 bar correction for elevation losses up to the cyclone.

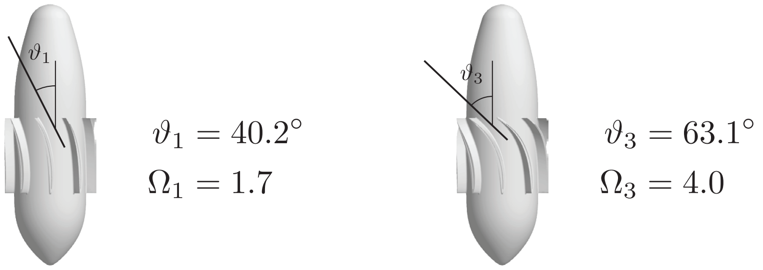

Figure 6.2: Geometry of swirl elements used in this thesis

Swirl element 1 has the lowest ratio of swirl to axial motion, which allows for an accurate study of the magnitude of U_θ required to produce a columnar flow. Swirl element 3 is the favoured geometry for experiments in the TOMOCON context. It produces relatively stable columnar flows for nearly all practical operating conditions, and was studied for comparison.

Low-range air flow controller

The air flow controller used in constructing the previous flow maps had a nominal range of 20–1000 Ln/min, but was clipped in practical operation around 250 Ln/min in order to avoid cavitation and air recycling in the setup [34]. Its accuracy however, was related to the full operating range: ±(0.5% MV + 1 Ln/min) [35]. Its use therefore led to significant measurement error at low gas flow rates.

As this thesis aims for understanding the asymptotic behaviour of swirling gas-liquid flows in the low-gas limit, the air flow controller was replaced with a 0–20 Ln/min model by the same supplier, intended for use with CO_2. It can be used for mass flow control of air by correcting the output voltage with a conversion factor 1.35, according to the specifications. This factor is based on a ratio of densities and specific heat capacities of both gases, which are assumed constant over the operating range [36]. This was implemented in LABVIEW.

With this adjustment, the setup allows for an accurate supply of 0–27 Ln/min of air to the input flow. In practical operation, this covers the entire bubbly flow range and the early onset of slug flow. In addition, it was considered beneficial to have some overlap with the minimum flow rates used in Ammerlaan's work, for a proper verification of data.

6.2 Extended flow maps

In line with Ammerlaan's research, the prevailing flow pattern for given input conditions is quantified visually in three locations: just upstream and just downstream of the swirl element, and prior to the outlets. Categorization is done based on the patterns discussed in chapter 2. Camera recordings were used to aid in distinguishing between patterns near a transition. In parallel to these visual observations, pressure and flow rate measurements are recorded with LABVIEW at a sampling rate of 2 Hz over 30 second intervals. This data is used to couple the occurrence of any pattern to the average superficial velocities:

$$j_{\mathrm{L}} = \frac{Q_{\mathrm{L}}}{A} \tag{6.1}$$

$$j_{\mathrm{G}} = \frac{Q_{\mathrm{G}}}{A}\left(\frac{p_a}{p_a + p_3}\frac{T}{T_0}\right) \tag{6.2}$$

$$\text{where} \quad p_a = 1.01325 \text{ bar}, \quad T_0 = 273.15 \text{ K}$$

The average gas flow rate Q_{G} is recorded in normal liters per minute (Ln/min), which are defined at atmospheric pressure and 0°C. The superficial gas velocity j_{G} therefore features a correction term based on the lab temperature and the pressure in the setup. The lab temperature is regulated to 20°C (293 K). The pressure in the separation section is estimated using the average gauge value just before the swirl element (sensor p_3). From this, the range of superficial velocities that can be covered with the setup is approximately

$$j_{\mathrm{L}} \;=\; 0.03 - 0.75 \text{ m/s} \qquad\qquad j_{\mathrm{G}} \;=\; 0.002 - 0.05 \text{ m/s}$$

The lower limit of j_{G} allows for extending the previous flow maps by roughly one order of magnitude below the minimum investigated by Ammerlaan. The range of j_{L} is equal.

It is noted here that the 'swirl dying' pattern categorized by Ammerlaan is not a true pattern, but a transition boundary. It signifies the outward breakup of any type of columnar flow due to instabilities, and cannot be sustained as a pattern. If conditions are such that a columnar flow can be sustained over longer distances, the point of breakup moves further downstream. Hence, where previous flow maps indicate 'swirl dying', this transition occurs exactly at the observed location. These data points are retained for continuity in the flow maps, but referred to as 'transverse breakup' in later chapters, to distinguish them from other transition mechanisms.

6.3 Differential pressure measurement

From a series of differential pressure measurements at various radial positions, it is possible to reconstruct the pressure profile $P(r)$. This can be used to obtain an estimate of the tangential velocity U_θ, since both are related by (4.33) — or, in integral form:

$$P(r) - P_0 \;=\; -\rho \int_r^R \frac{U_\theta^2}{r}\,\mathrm{d}r \tag{6.3}$$

Here, the left-hand side is the differential pressure to be obtained, with P_0 the static wall pressure. The latter can be monitored with a fixed pressure sensor connected to the inside of the pipe wall. To obtain $P(r)$, an simple intrusive sensor was designed, which employs teflon fittings to allow for adjusting its radial position in the flow.

The geometry of the sensor is illustrated in figure 6.3. It is fabricated from ∅ 3 mm hollow stainless steel tubing, which is bent upward over a length of 60 mm. This length serves for better streamwise flow development at the measurement position, after its initial distortion by the transverse section of the tube. The tube end is sealed with a slotted head screw, glued in. At 50 mm, a ∅ 1.5 mm sensing hole was made in the tube wall, on the opposing side of where the sensor obstructs the flow. This allows for near-static pressure measurements in the radial direction, because $U_r \sim 0$ implies any dynamic pressure component will have a negligible magnitude. This argument does not hold for sensing along the $\hat{\theta}$ and $\hat{z}$ directions, because the velocity components U_θ and U_z are significant.

Two inset pipe sections were fitted with sensor throughputs on opposite sides of their perimeter, spaced 50 mm apart in the steamwise direction, to allow for measurement of $P(r)$ and P_0 at the same reference height z. This requires correcting the magnitude of $P(r)$ for the static pressure of the fluid column inside the sensor, as indicated in figure 6.3. If the sensor is in the upright position, this column is near 100% liquid even for measurements on gas-liquid flows: if gas is taken up in the sensor at all, it cannot push out the liquid below.

These pipe sections were installed just after the swirl element ($z/D = 2.5$) and prior to the outputs ($z/D = 15.2$), so that pressure measurements could be made in the same locations that were observed for the flow maps. This also allows for obtaining coarse estimates of the axial pressure gradient and the decay of U_θ.

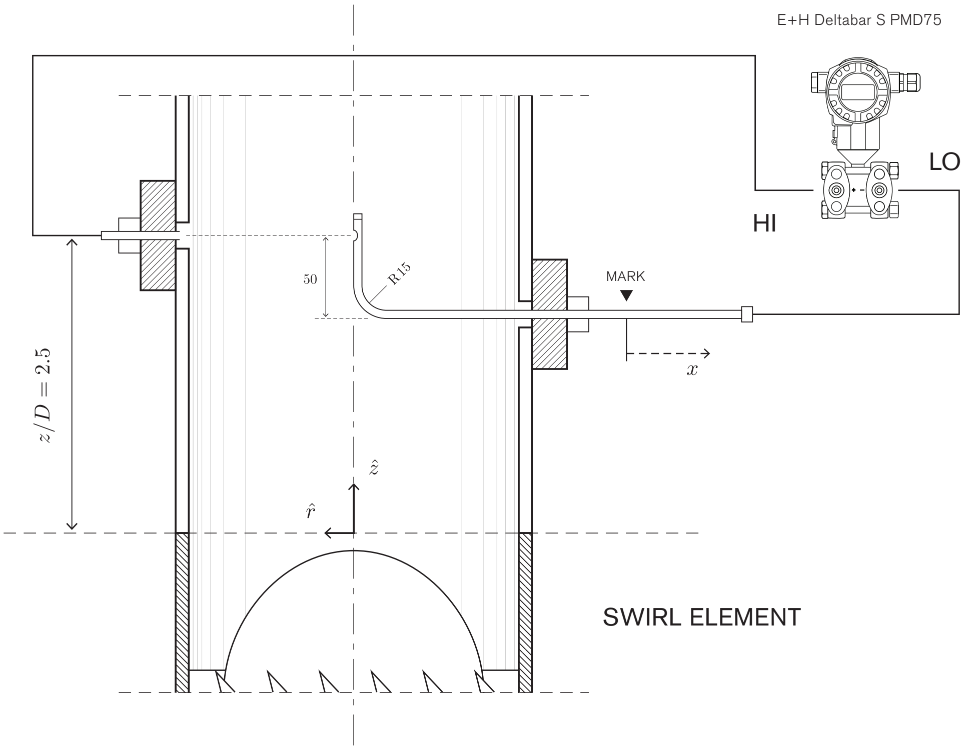

Figure 6.3: Differential pressure measurement setup, using a fixed wall sensor (left) and an adjustable intrusive sensor tube (right). The illustration shows the measurement location just downstream of the swirl element.

Differential pressure data was obtained with an Endress+Hauser Deltabar S transmitter, model PMD75, through an extension of the LABVIEW routine. Its HI input was connected to the inner wall and its LO input to the intrusive sensor, using flexible tubing. This model allows for correcting the hydrostatic offset on the device. To this end, the separation section was filled with a static, non-swirling liquid column before every operation. After flushing all tubing to remove any remaining air, the offset was corrected.

The device has different operating ranges from -30 ... 30 mbar to -3 ... 3 bar, with total measurement error listed as 0.05% of the adjusted span. Depending on the flow rates used, the measurement span varied from 0 to 30–75 mbar in this thesis. The device output current is 4–20 mA, which is converted by a small DC circuit to 2–10 V. Any voltage X therefore relates to a differential pressure dependent on the span boundaries as follows:

$$\Delta P \; = \; \frac{X-2}{10-2}\Big(\textsc{max} - \textsc{min}\Big) + \textsc{min} \tag{6.4}$$

A reference mark was made on a part of the sensor that remained outside the separator, indicating centerline alignment of the upward part. Measurements at various radial positions were related to this reference mark using a high-precision caliper. All differential pressure data was averaged over 30 measurements after acquisition (2 Hz, 15 s).

6.4 Data fitting

A fit model was constructed for the differential pressure measurements, based on (6.3). This required an a priori assumption on the general form of the tangential velocity profile U_θ, since the right-hand side integral does not allow for data fitting directly. As a best guess based on previous observations, the Gaussian vortex profile (equation (5.1)) was employed. This appeared to fit the data with high accuracy. Evaluating the integral yields a semi-analytical fit expression for $P(r)$:

$$P(r) \;=\; P_0 - \frac{1}{2}\rho U_\theta^2 - \rho B^2 \frac{\gamma}{R_c^2} \left\{ E_1\Big(\gamma(r/R_c)^2\Big) - E_1\Big(2\gamma(r/R_c)^2\Big) \right\} \tag{6.5}$$

Here, $E_1(x)$ is the exponential integral, with x as its lower limit:

$$E_1(x) \;=\; \int_x^\infty \frac{e^{-t}}{t}\,\mathrm{d}t \tag{6.6}$$

The above is a three parameter fit model for $P(r)$, based on the quantities $(B,\, R_c,\, P_0)$. These respectively fix the magnitude and spread of the tangential velocity profile, and the constant offset due to the static wall pressure. After fitting the pressure data, substitution of B and R_c in (5.1) yields an estimate of the tangential velocity profile.

In the absence of data on the mixture density $\widetilde{\rho}$, the liquid density ρ_L was used in (6.5) as a first-order estimate for processing all measurements. In the low-gas limit, this is a reasonable approximation. At higher gas flow rates however, this might incur significant error in the fit parameters B, R_c, and P_0. It should be further investigated if results obtained with the modelling framework can provide a good estimate of $\widetilde{\rho}$ in these cases.

Chapter 7

Experimental results

This chapter presents experimental data on swirling air-water flows obtained with the TOMOCON setup, to facilitate a comparison between the modelling output and previous observations. Section 7.1 features extended flow maps for swirl elements 1 and 3. These are composite maps of new data and previous work that was verified as part of this thesis. Radial pressure profiles under various operating conditions are discussed in section 7.2, and estimates for the tangential velocity $U_\theta(r)$ are presented. Throughout this chapter, it is questioned whether these results can provide verification of the modelling framework developed in chapter 4.

7.1 Extended flow maps

Figure 7.2 and 7.3 depict the extended flow maps for swirl element 1 and 3 respectively, at locations just downstream of the cyclone and prior to the outlets. Indicators along the horizontal axis signify the range of superficial gas velocities over which new or previous data (from [34]) is used. The occurrence of columnar flow patterns at given input conditions is illustrated with filled markers, For non-columnar flows, open markers are used.

Empirical transition curves separating columnar and non-columnar flow patterns are superposed on these maps and labeled for further discussion in section 7.1.1. Throughout all flow maps, these curves show a downward trend in the bubbly flow range when moving towards lower gas flow rates. A constant j_L threshold for transition to columnar flows therefore does not correctly represent the underlying physics in the low-gas limit. For input flows in the slug and churn range however, this remains a valid criterion.

Data points near the minimum gas flow rates investigated by Ammerlaan (marked $*$) did not correctly classify the flow for values of j_L around the transition. This was most notable just downstream of swirl element 1. The data in this range have been replaced by new measurements obtained with the low-range gas flow controller.

7.1.1 A two-stage transition from bubbly to columnar flow

An important observation in the bubbly flow range is the occurrence of non-homogeneous bubble distributions downstream of the swirl element, prior to the formation of a fully columnar flow. Figure 7.1 shows three different photographs of such distributions. Here, all gas content over a certain inner region of the pipe gathers along the centerline into a semi-column of closely packed, but discrete bubbles. Outside this region, individual bubbles rise upward freely along a helical trajectory. This is attributed to the centrifugal forces not being strong enough in the outside region to direct these bubbles inward.

This behaviour resembles the clustered bubbly pattern discussed in chapter 2 (albeit without the outer bubbles), and is therefore categorized as such in the flow maps.

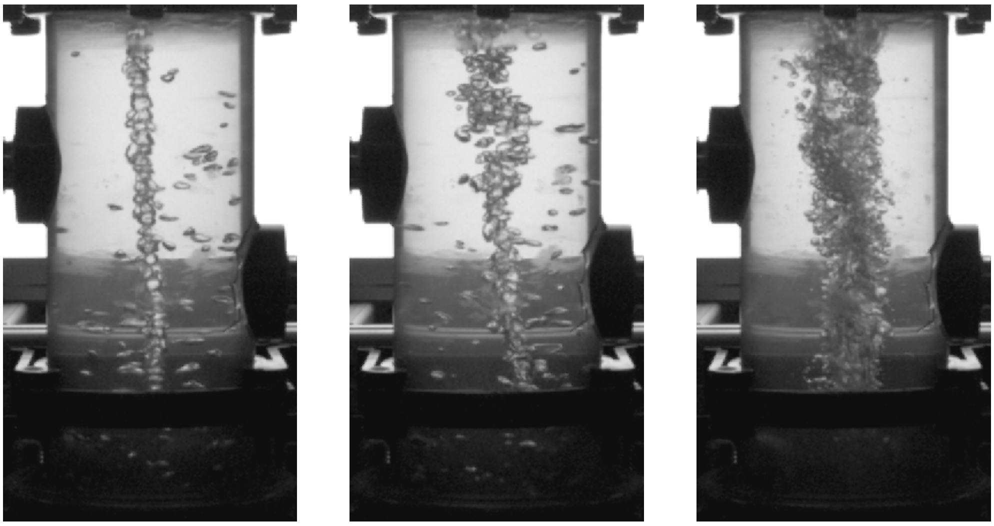

(a) 2 Ln/min (b) 3 Ln/min (c) 15 Ln/min

Figure 7.1: Snapshots of the clustered bubbly pattern observed in the TOMOCON setup for various gas flow rates

The clustered bubble semi-columns are clearly visible at low gas flow rates. At increased (but still homogeneous) bubble concentrations this behaviour pertains, but it becomes more difficult to distinguish the cluster because the abundance of individual bubbles in the outer region obstructs the view towards the centerline. As gas flow rates approach the slug range, the input flow is no longer homogeneous: it contains incidental larger bubbles that break the fragile bubble cluster in passing. Consequently, the clustered bubbly pattern disappears around $j_{\mathrm{G}} = 0.06$ m/s in both downstream flow maps.

At increased superficial liquid velocity, bubble clusters coalesce into columnar flows, and full separation of phases results. Values of j_{L} required for coalescence increase with j_{G} throughout the bubbly flow range, up to the thresholds defined previously by Ammerlaan. Based on these observations, it is proposed that the transition from bubbly to columnar flow is a two-stage process:

1. *Clustering:* this transition is labeled 'A' in figures 7.2 and 7.3, and appears to have a constant threshold depending on the swirl element:

$$\begin{aligned} j_{\mathrm{L}} &= 0.125 \text{ m/s} \qquad \text{for swirl element 1} \\ j_{\mathrm{L}} &= 0.055 \text{ m/s} \qquad \text{for swirl element 3} \end{aligned}$$

   The product of these thresholds with the swirl intensity Ω is a rough measure of U_θ, i.e. the total amount of swirl induced, which appears to be equal for both flow maps.

   Bubble clustering is absent in the flow maps prior to the outlets because this pattern cannot be sustained over great lengths in practice before coalescence occurs. For most data points near the outlets that are labeled bubbly, a columnar flow exists upstream, but it has broken up before the observation area due to swirl decay.

2. *Coalescence:* this transition is indicated by 'B' in all flow maps. On a qualitative basis, it appears sensible that higher gas concentrations require larger centripetal forces for a columnar flow to occur: the total surface tension forces to be overcome increase with the number of bubbles that need to coalesce. In the axial cyclone separator, the centripetal forces are related to the input momentum, which is predominantly due to the liquid velocity — i.e. j_{L}. It would be interesting to quantify this transition by a Weber number (inertia : surface tension), as discussed in section 5.1.1.

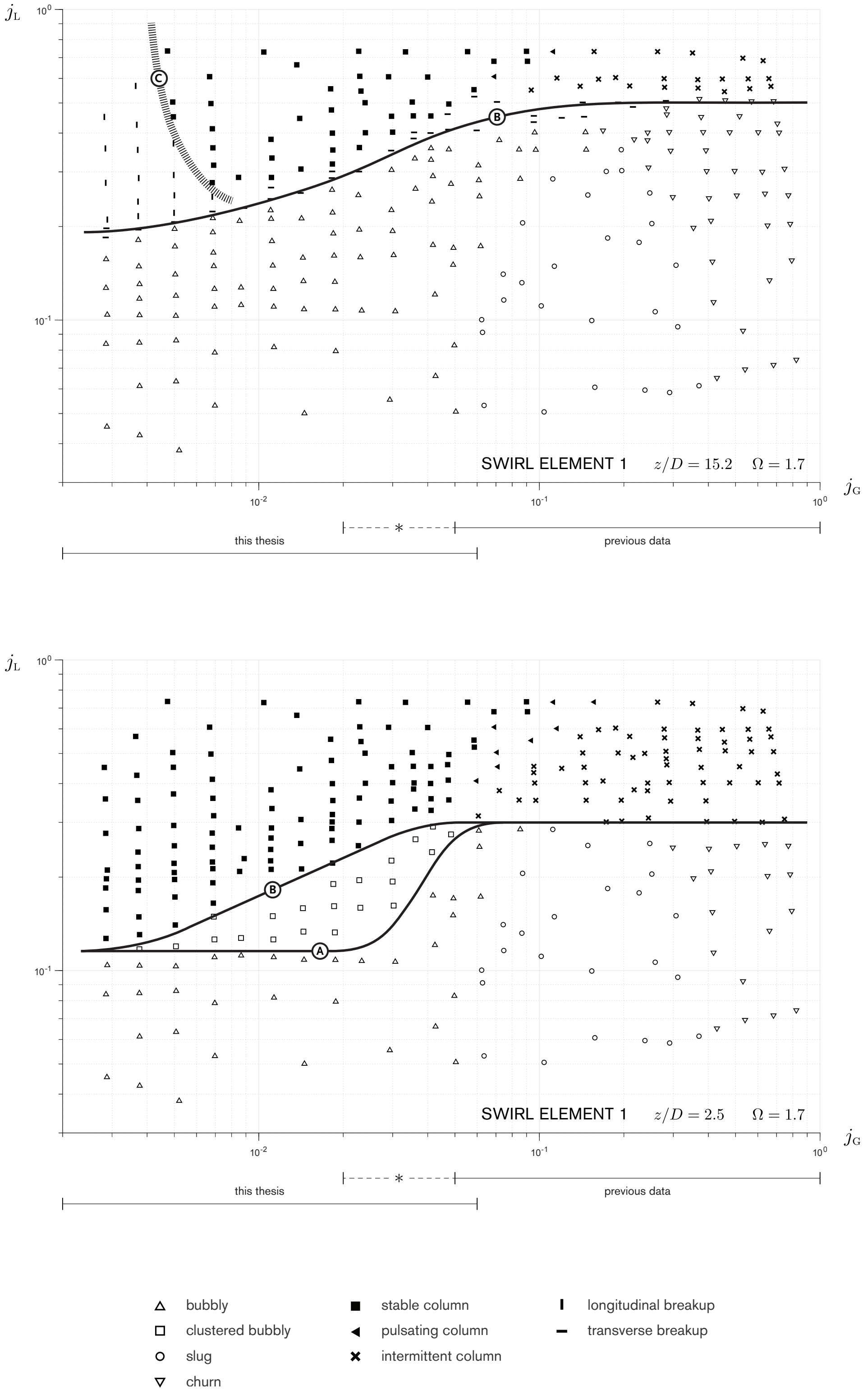

Figure 7.2: Extended flow maps for swirl element 1, prior to the outlets (top) and downstream of the swirl element (bottom)

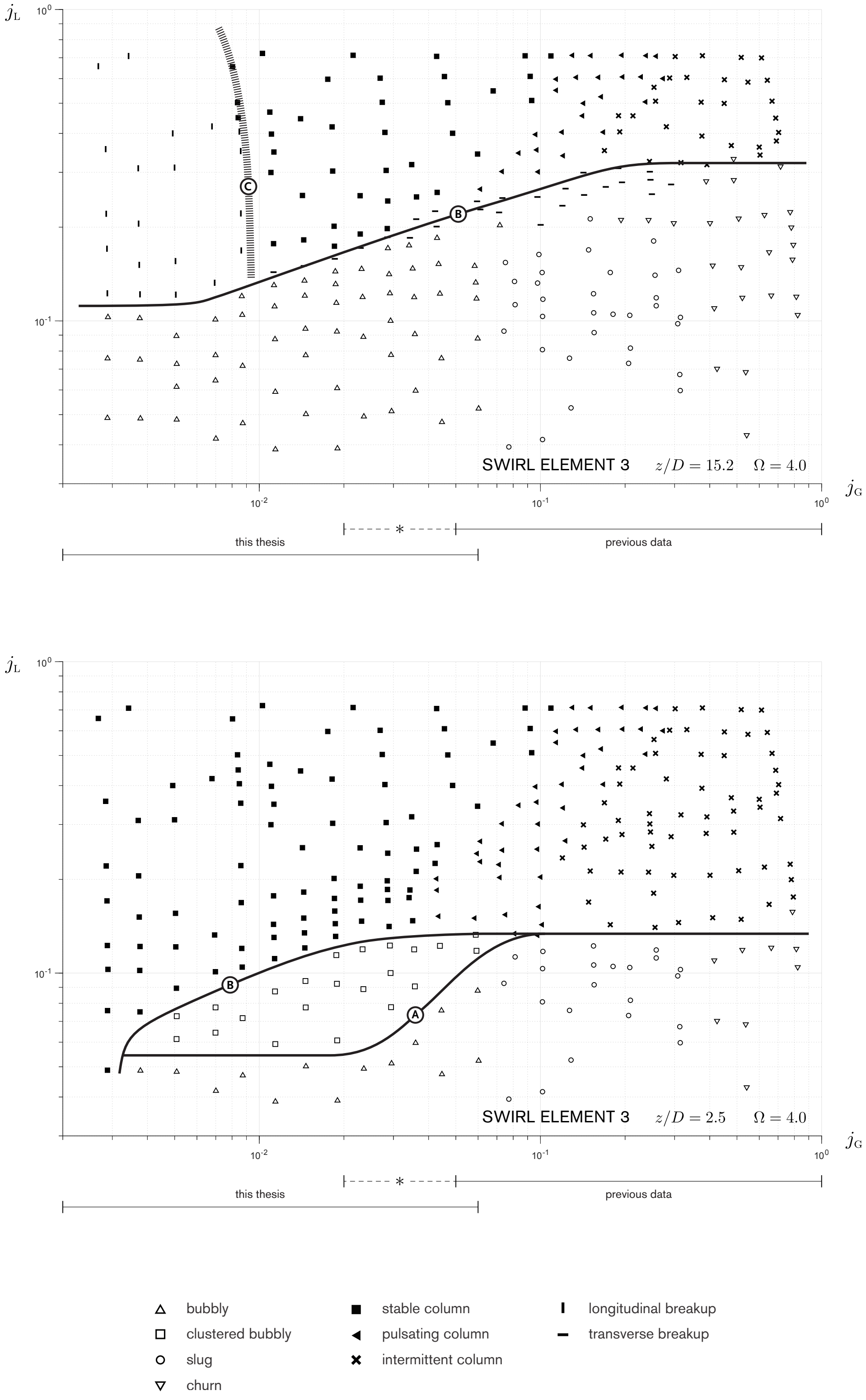

Figure 7.3: Extended flow maps for swirl element 3, prior to the outlets (top) and downstream of the swirl element (bottom)

The modelling output discussed in chapter 5 appears to be representative of both transition mechanisms. Its predicted non-homogeneous distributions of α_G even at low magnitudes of U_θ agree with the observed clustered bubbly patterns at low flow rates. The limited presence of bubbles in the outer region is not reflected in the output, but this can be explained.

The modelling framework is focused on force mechanisms that prevail in the core of the flow. Effects occurring in the near-wall region were not included. For gas-liquid flows without swirl however, several authors have shown that a balance of lift and wall forces leads to a characteristic peak in bubble concentration near the wall [11, 13]. This behaviour was estimated insignificant in the case of swirling flow for most practical operating conditions. But at the low swirl intensities that lead to the clustered bubbly pattern, the inclusion of near-wall force mechanisms should correctly predict the presence of the outer bubbles.

It also seems plausible that a threshold can be formulated on the basis of the gas fraction distribution to predict the onset of coalescence. As discussed in section 5.1.1 however, a better approach towards a quantitative criterion would be to extend the current model to account for collision effects.

7.1.2 Longitudinal breakup

For columnar flow patterns at low gas flow rates, the centerline column is very thin. In such cases, instabilities were observed that break the columnar pattern into distinct columnar sections, travelling downstream. These instabilities prevail over a wide range of j_L and are denoted as 'longitudinal breakup' in the flow maps. The associated transition curve 'C' is deliberately illustrated with a wide dashed line, because the physics behind it is not well understood at this point.

It it assumed that oscillations in the liquid annulus (which increase in both frequency and magnitude with j_L) can 'choke' the thin columnar flow, causing breakup. Because the centripetal forces are still strong given the associated velocities, a columnar flow re-forms soon after, and the flow visually appears as a series of distinct columnar sections.

Longitudinal breakup starts near the outlets but soon after affects the flow over the entire length of the separation section. Further research in this area could clarify its origins, but this is not of direct practical interest in the TOMOCON context.

7.2 Radial pressure profiles

7.2.1 For swirl element 1

Figures 7.4–7.5 show pressure profiles for swirl element 1 for various operating conditions. A fit of the data using equation (6.5) is superposed on the graphs. To allow for comparison between different gas flow rates, the superficial mixture velocity j $(= j_\mathrm{L} + j_\mathrm{G})$ is used as a fixed parameter. The marker type in each graph is indicative of both gas flow rate and superficial mixture velocity.

Just downstream of swirl element 1 ($z/D = 2.5$) a large difference in magnitude of the pressure profile is observed between single-phase liquid flow and mixture flows of various gas content. This behaviour was unexpected and is assumed to be related to the complex dynamics inside the swirl element. From figure 7.4, a comparison between 0 Ln/min (a) and 12 Ln/min (b) flows over a range of mixture velocities indicates ΔP can differ up to a factor 2 at the centerline. There is a non-linear dependence on the mixture velocity.

The gas presence appears to increase the radial pressure gradient, leading to a stronger separation of phases cf. section 4.2.2. Profiles of various gas flow rates both downstream and prior to the outlets ($z/D = 15.2$) illustrate that this holds true up to a certain maximum j_G, after which the pressure gradient is reduced again, even below its single-phase magnitude for gas flow rates around 21 Ln/min. Near the outlets, the spread between profiles is notably less, supporting the assumption that this behaviour is related to the swirl element.

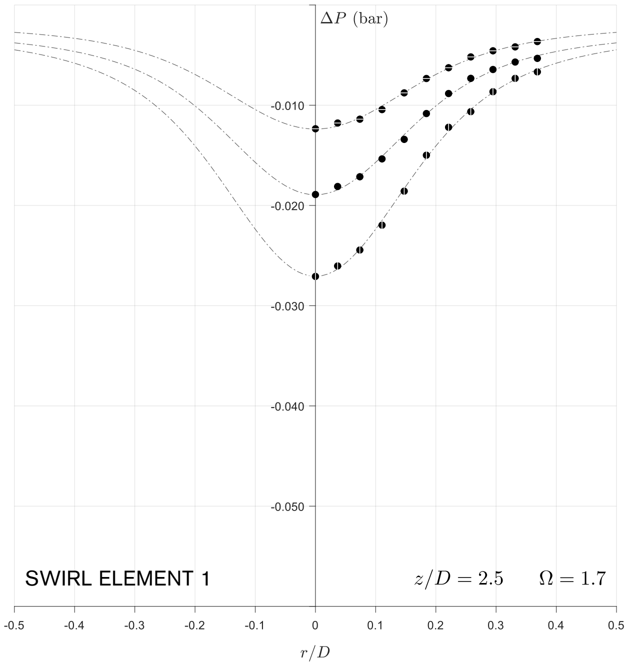

(a) 0 Ln/min — single-phase

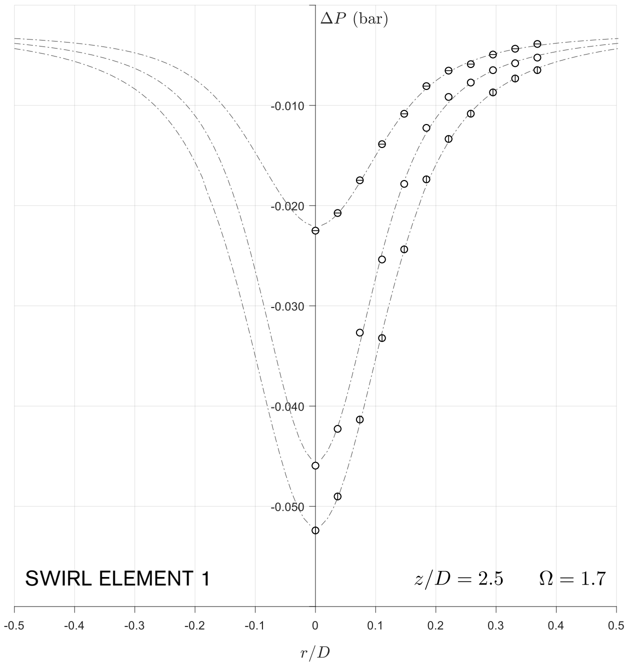

(b) 12 Ln/min — $j_{\mathrm{G}} = 0.033$ m/s

Figure 7.4: Radial pressure profiles for swirl element 1 at various superficial mixture velocities: 0.5 m/s (◓/⊖), 0.6 m/s (●/○), 0.7 m/s (◐/⦶),

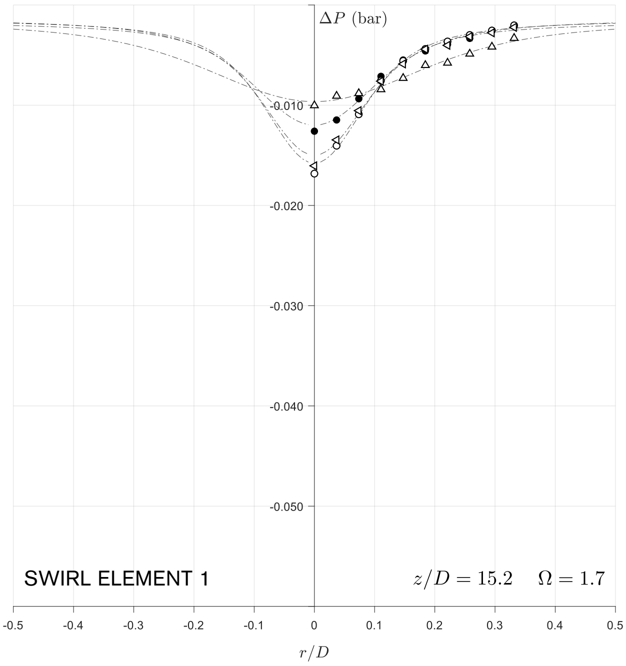

(a) prior to outlets

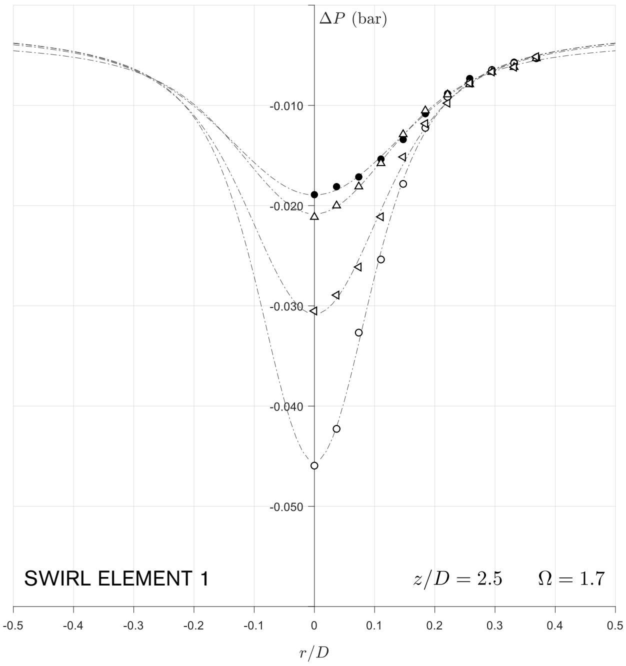

(b) downstream of swirl element

Figure 7.5: Radial pressure profiles for swirl element 1 at various gas flow rates, $j = 0.6$ m/s. 0 Ln/min (●), 3 Ln/min (◁), 12 Ln/min (○), 21 Ln/min (△)

input		$z/D = 2.5$		$z/D = 15.2$	
Ln/min	j_{G} (m/s)	B/j_{L}	R_c/D	B/j_{L}	R_c/D
0	0	0.038	0.20	0.019	0.13
3	0.008	0.037	0.15	0.019	0.11
12	0.033	0.038	0.13	0.019	0.10
21	0.060	0.036	0.17	0.034 †	0.23 †

Table 7.1: Fit parameter estimates for swirl element 1 data in figure 7.5, from which U_θ can be recovered. Data marked † appear anomalous.

Estimates of U_θ

The fit model resulting from a Gaussian vortex U_θ provides a good fit to the measurements done on swirl element 1, for all mixture compositions. Table 7.1 lists the values of fit parameters B and R_c obtained for the data in figure 7.5, both downstream of the swirl element and prior to the outlets. These parameters have been normalized by the superficial liquid velocity and pipe diameter respectively.

Notably, B/j_{L} appears to have constant magnitude irrespective of the gas flow rate. The differences in $P(r)$ observed in figure 7.5b are solely caused by the core radius R_c/D: increased gas flow rates shift its magnitude to lower values (up to the maximum described previously, after which it increases again). Data marked with † are an outlier with respect to this trend, and should be reinvestigated.

Physically, the parameter B is related to the circulation (area integral of vorticity), which can be regarded as a measure of the swirl intensity. In this respect, constant values for B/j_{L} appear a correct reflection of the use of swirl elements of fixed Ω.

These estimates of U_θ closely align with the input conditions used in the solving routine, cf. figure 5.1a. In the experiments however, the swirl intensity is notably higher. This indicates that these magnitudes of U_θ occur in conjunction with lower axial velocity U_z than calculated in section 5.2.

Estimate of swirl decay parameter ξ

The fit data in table 7.1 can also be used to construct an estimate of the swirl decay in the setup. Because of the observed reduction in R_c between both measurement locations, exponential decay of the area integral of U_θ (a lumped quantity) is considered, i.e.

$$\left[\iint U_\theta \, r \, \mathrm{d}r \, \mathrm{d}\theta\right] e^{-\xi(z/D)}$$

This yields $\xi = 0.043$ for swirl element 1, in agreement with its expected order of magnitude. There is a factor 2 difference with the input value used in the solving routine. This indicates the influence of swirl decay on the axial pressure gradient is larger than the estimates in figure 5.1b, i.e. the reduction near the centerline is more pronounced in practice.

7.2.2 For swirl element 3

Figures 7.6–7.7 show pressure profiles obtained for swirl element 3 under similar operating conditions. There are strong differences in behaviour in comparison to swirl element 1. Again, this was unexpected. In terms of relative magnitude, the observed ΔP for swirl element 3 are larger. However, no significant increase in the radial pressure gradient occurs over the range of gas flow rates investigated. The efficiency of separation is therefore not affected by the magnitude of j_G, as it is for swirl element 1.

Just downstream of swirl element 3 ($z/D = 2.5$), figure 7.6 illustrates two distinct regions in the pressure profile of both single-phase and 12 Ln/min mixture flows. A region of near-linear trend extends from the centerline up to $R_c \sim 0.15D$. Its slope is relatively flat in the case of single-phase flow, and more inclined for the mixture flow. Outside this region, data appears in agreement with the trend predicted by the fit model. Consequently, the tangential velocity profile does not fully resemble a Gaussian vortex here. Figure 7.7a indicates that measurements near the outlets ($z/D = 15.2$) do agree with the fit model, and these curves have been superposed on the graph.

Recirculation could be a possible explanation for this behaviour. It is plausible that the strong swirling motion incurred by swirl element 3 leads to regions of adverse axial pressure gradient near the centerline. The resulting backflow transports fluid with low swirl from near the outlets down towards the swirl element, which leads to a local damping of the radial pressure gradient. The geometry of the swirl element (figure 6.2b) implies that its high swirl output is injected into the separation section in a wall-jet like manner. The simultaneous occurrence of recirculation and injection then accounts for the distinct regions observed in the pressure profiles.

Backflow has been observed under practical operating conditions. However, additional research is required to fully test this hypothesis.

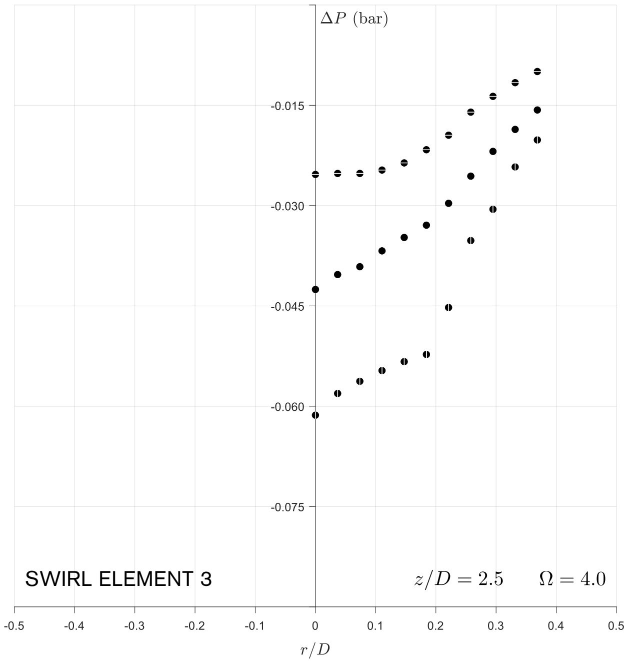

(a) 0 Ln/min — single-phase

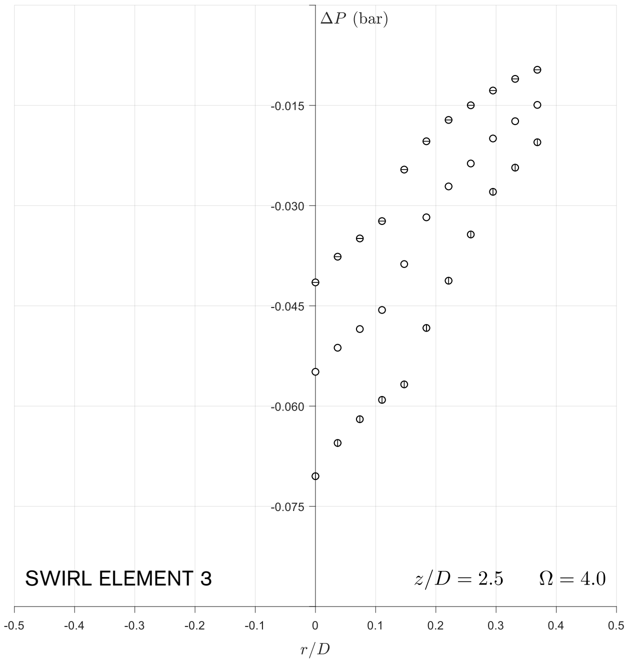

(b) 12 Ln/min — $j_{\mathrm{G}} = 0.033$ m/s

Figure 7.6: Radial pressure profiles for swirl element 3 at various superficial mixture velocities: 0.5 m/s (◒/⊖), 0.6 m/s (●/○), 0.7 m/s (◐/⦶),

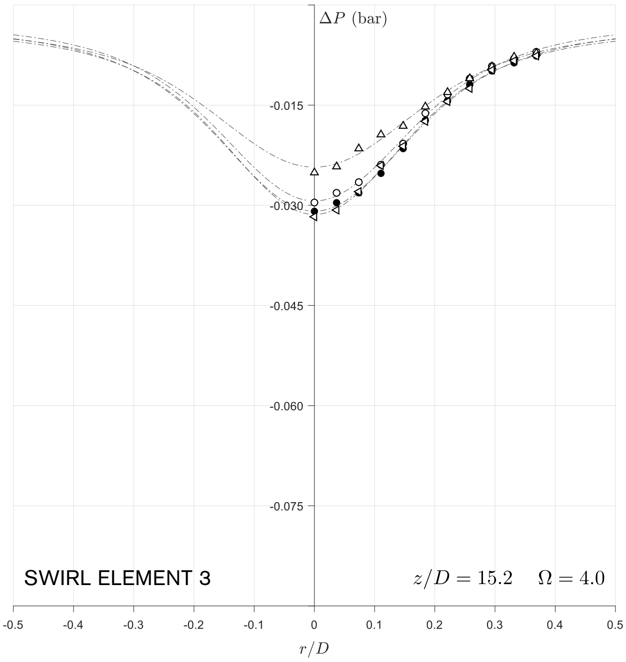

(a) prior to outlets

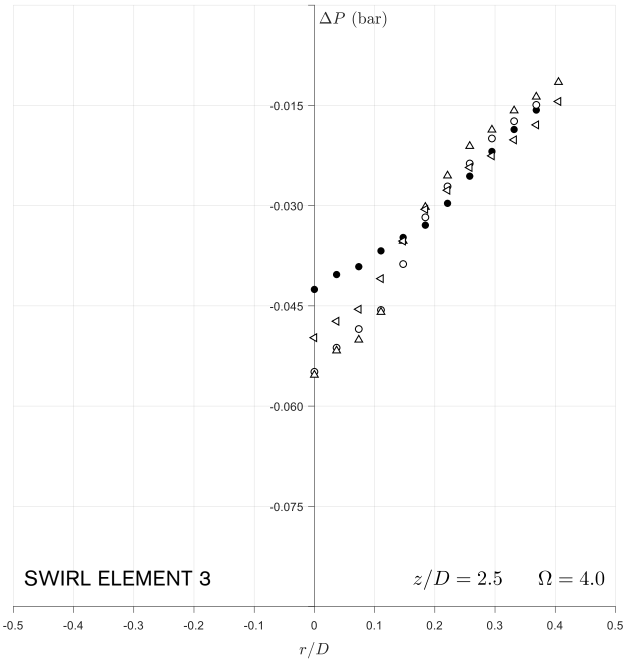

(b) downstream of swirl element

Figure 7.7: Radial pressure profiles for swirl element 3 at various gas flow rates, $j = 0.6$ m/s. 0 Ln/min (●), 3 Ln/min (◁), 12 Ln/min (○), 21 Ln/min (△)

Chapter 8

Conclusion

This thesis aimed for developing a mechanistic modelling framework for swirling gas-liquid vertical pipe flow, with the intention to produce relatively accurate predictions of the flow dynamics with limited means. As a benchmark case, this modelling framework was used to investigate the onset of columnar flow patterns for low gas input flows.

Experimental data obtained with an inline swirl separator for similar input indicate that the transition from bubbly to columnar flow is a two-stage process, characterized by clustering and subsequent coalescence of the gas phase near the pipe centerline. Clustering starts from a constant, low rate of swirl, while the onset of coalescence occurs at higher tangential velocities and depends on the gas fraction. Previous research identified only the coalescence stage, and noted a constant superficial liquid velocity threshold for transition. This appears to hold true only for gas flow rates corresponding to slug and churn input.

The modelling framework seems to provide a correct reflection of the non-homogeneous distribution of phases that is associated with clustering. It is based on the assumption of non-zero, but negligible streamwise derivatives (a quasi-1D approach). This assumption appears valid only when the effects of swirl decay on the radial distribution of the axial pressure gradient are small. For practical operation of swirl separators, it implies limited model applicability because such effects are significant. The inclusion of exponential swirl decay as the only relevant streamwise variation yields promising results over a wider range of input conditions. Qualitative agreement was obtained between model predictions for the streamwise velocity and observations on single-phase flow in the literature.

This implies that the dynamics of a swirling flow can be correctly captured with simple models and a limited number of input parameters (wall pressure gradient, decay constant, gas concentration and tangential velocity). For the latter, pressure measurement fitting verified that a Gaussian vortex velocity profile is a good assumption at low swirl intensities, where backflow does not occur. A simple iterative solver loop was constructed in MATLAB to illustrate the modelling output. An important aspect in the context of process control for swirl separation is that this solver loop generates predictions fast. The modelling framework is therefore suitable for use in near real-time control strategies.

On the basis of the modelling output, a qualitative transition criterion for the bubbly to columnar flow transition was formulated, using the α_{G} threshold of the bubbly to slug transition in regular gas-liquid flow. This seems a valid analogy as both transitions are characterized by clustering and coalescence — the difference in swirling flow being that these are forced to occur in a limited region of the pipe only. It is recommended that this transition is studied further using a collision model, to be able to explain the onset of coalescence from physical reasoning.

Outlook

Currently, the solver loop converges for limited swirl intensities only because it is based on disperse flow reasoning. This can be addressed by developing a separated flow implementation of the same modelling framework. This is a key extension of the ideas developed in this thesis, that is recommended for further research. In principle, it would allow for using the modelling framework in the context of high gas content input flows (slug, churn) and for quantification of the transitions to pulsating and intermittent columnar flow patterns.

To further coordinate the disperse flow implementation of the modelling framework to observations, and quantify the transition from bubbly to stable columnar flow, it is recommended to construct an additional swirl element, which produces a swirl intensity in the range of convergence of the model ($\Omega \lesssim 1$).

Appendix A

Expanded equations

This section lists the full expansion of the individual phase conservation equations for turbulent multiphase flow, which were presented in simplified form (only terms relevant to swirling flow retained) in section 4.1.4. These are ensemble-averaged equations for the mean flow in a cylindrical coordinate basis. Effects of molecular viscosity are not taken into account here. These can be added onto these equations whenever relevant.

Mass conservation equation (4.3)

$$\frac{\partial}{\partial t}\big(\alpha_{\mathrm{N}}\rho_{\mathrm{N}}\big) + \frac{1}{r}\frac{\partial}{\partial r}\big(r\,\alpha_{\mathrm{N}}\rho_{\mathrm{N}}U_{\mathrm{N}r}\big) + \frac{1}{r}\frac{\partial}{\partial \theta}\big(\alpha_{\mathrm{N}}\rho_{\mathrm{N}}U_{\mathrm{N}\theta}\big) + \frac{\partial}{\partial z}\big(\alpha_{\mathrm{N}}\rho_{\mathrm{N}}U_{\mathrm{N}z}\big) \;=\; 0$$

Momentum conservation equations (4.4)

radial direction (r):

$$\begin{aligned}
\alpha_{\mathrm{N}}\rho_{\mathrm{N}}\frac{\partial U_{\mathrm{N}r}}{\partial t} + \alpha_{\mathrm{N}}\rho_{\mathrm{N}}\left(U_{\mathrm{N}r}\frac{\partial U_{\mathrm{N}r}}{\partial r} + \frac{U_{\mathrm{N}\theta}}{r}\frac{\partial U_{\mathrm{N}r}}{\partial \theta} + U_{\mathrm{N}z}\frac{\partial U_{\mathrm{N}r}}{\partial z} - \frac{U_{\mathrm{N}\theta}^2}{r}\right) \;=&\\
-\alpha_{\mathrm{N}}\frac{\partial P}{\partial r} + \big\langle \mathcal{F}_{\mathrm{N}r}\big\rangle - \frac{1}{r}\frac{\partial}{\partial r}\left(r\,\alpha_{\mathrm{N}}\rho_{\mathrm{N}}\,\overline{u'^2_{\mathrm{N}r}}\right) - \frac{1}{r}\frac{\partial}{\partial \theta}\left(\alpha_{\mathrm{N}}\rho_{\mathrm{N}}\,\overline{u'_{\mathrm{N}r}u'_{\mathrm{N}\theta}}\right) \;+&\\
\frac{\overline{u'^2_{\mathrm{N}\theta}}}{r} - \frac{\partial}{\partial z}\left(\alpha_{\mathrm{N}}\rho_{\mathrm{N}}\,\overline{u'_{\mathrm{N}r}u'_{\mathrm{N}z}}\right)&
\end{aligned}$$

tangential direction (θ):

$$\begin{aligned}
\alpha_{\mathrm{N}}\rho_{\mathrm{N}}\frac{\partial U_{\mathrm{N}\theta}}{\partial t} + \alpha_{\mathrm{N}}\rho_{\mathrm{N}}\left(U_{\mathrm{N}r}\frac{\partial U_{\mathrm{N}\theta}}{\partial r} + \frac{U_{\mathrm{N}\theta}}{r}\frac{\partial U_{\mathrm{N}\theta}}{\partial \theta} + U_{\mathrm{N}z}\frac{\partial U_{\mathrm{N}\theta}}{\partial z} + \frac{U_{\mathrm{N}r}U_{\mathrm{N}\theta}}{r}\right) \;=&\\
-\frac{\alpha_{\mathrm{N}}}{r}\frac{\partial P}{\partial r} + \big\langle \mathcal{F}_{\mathrm{N}r}\big\rangle - \frac{1}{r^2}\frac{\partial}{\partial r}\left(r^2\,\alpha_{\mathrm{N}}\rho_{\mathrm{N}}\,\overline{u'_{\mathrm{N}\theta}u'_{\mathrm{N}r}}\right) \;-&\\
\frac{1}{r}\frac{\partial}{\partial \theta}\left(\alpha_{\mathrm{N}}\rho_{\mathrm{N}}\,\overline{u'^2_{\mathrm{N}\theta}}\right) - \frac{\partial}{\partial z}\left(\alpha_{\mathrm{N}}\rho_{\mathrm{N}}\,\overline{u'_{\mathrm{N}\theta}u'_{\mathrm{N}z}}\right)&
\end{aligned}$$

axial direction (z):

$$\begin{aligned}\alpha_{\mathrm{N}}\rho_{\mathrm{N}}\frac{\partial U_{\mathrm{N}z}}{\partial t}+\alpha_{\mathrm{N}}\rho_{\mathrm{N}}\left(U_{\mathrm{N}r}\frac{\partial U_{\mathrm{N}z}}{\partial r}+\frac{U_{\mathrm{N}\theta}}{r}\frac{\partial U_{\mathrm{N}z}}{\partial \theta}+U_{\mathrm{N}z}\frac{\partial U_{\mathrm{N}z}}{\partial z}\right) &= \\ -\alpha_{\mathrm{N}}\rho_{\mathrm{N}}g-\alpha_{\mathrm{N}}\frac{\partial P}{\partial z}+\left\langle\mathcal{F}_{\mathrm{N}z}\right\rangle-\frac{1}{r}\frac{\partial}{\partial r}\Big(r\,\alpha_{\mathrm{N}}\rho_{\mathrm{N}}\,\overline{u'_{\mathrm{N}z}\,u'_{\mathrm{N}r}}\Big) &- \\ \frac{1}{r}\frac{\partial}{\partial \theta}\Big(\alpha_{\mathrm{N}}\rho_{\mathrm{N}}\,\overline{u'_{\mathrm{N}z}\,u'_{\mathrm{N}\theta}}\Big)-\frac{\partial}{\partial z}\Big(\alpha_{\mathrm{N}}\rho_{\mathrm{N}}\,\overline{u'^{2}_{\mathrm{N}z}}\Big)\end{aligned}$$

Appendix B

Solving routine code (MATLAB)

```
clc
clearvars
close all


% INCLUDE variables
vars


% BOUNDARY CONDITIONS: fixed throughout
% --------------------
jG   = 0.01;                         % superficial gas velocity (m/s)

% gaussian vortex input
y    = 1.256;
Rc   = 0.2 * D;
Uth  = 0.04 * ( 1 - exp( -y * (r/Rc).^2 ) ) ./ r;

% radial variation of dpdz
pv   = cumtrapz( dr, rhoL * Uth.^2./r );
pv   = pv - pv(end);

dpdz = -(1.065 * rhoL*g) - 0.5 * pv; % pressure gradient (Pa/m)


% PRE-LOOP CONDITIONS: to initiate iteration
% --------------------
aL = ones(dim);                      % liquid holdup
Uz = ones(dim);                      % axial velocity: plug flow
Uc = Uz;                             % core velocity profile

b  = 0.13;
L  = b * (D/2);                      % integral length scale
vt = L^2 * (Uz / D);                 % eddy viscosity (mixing length model)
Sc = 1;                              % turbulent Schmidt number

Cl = 0.3;                            % lift coefficient (Tomiyama correlation)


Re = @(v) d * rhoL/muL * abs(v);     % bubble Reynolds number
Cd = @(v) max( 0.44, ...
               24./Re(v) .* (1 + 0.15*Re(v).^0.687) );
```

```
% LOOP START
% -------------------

for i = 1:30

% A. auxiliary parameters
Dt = vt / Sc;                        % turbulent dispersion coefficient


% B. gas-liquid slip velocity
ig   = 0.25 * ones(dim);             % initial guess
lb   = zeros(dim);                   % lower bound
ub   = realmax * ones(dim);          % upper bound

zbal = @(v)  v.^2 - 4/3 * d ./ (rhoL * aL .* Cd(v)) .* ( -dpdz - rhoG*g );
U0   = lsqnonlin(zbal, ig, lb, ub);


% C. gas fraction profile aG(r)
% integrating factors: dispersion, lift
ifd  = 4/3 * d * (rhoL-rhoG)/rhoL * ...
                      cumtrapz( dr, Uth.^2 ./ (Cd(U0) .* Dt .* U0 .* r) );
ifl  = 4/3 * d * Cl * cumtrapz( dr, gradient(Uc,dr) ./ (Cd(U0) .* Dt) );

% analytical solution
aG   = @(c)  c ./ ( exp(ifd).*exp(ifl) + c );

% set free parameter by integral condition: jG
cr   = [0 realmax];   % to enforce positive solution
intb = @(c)  jG - 1/A * ( 2 * pi * trapz( dr, aG(c) .* (Uz + U0) .* r ) );

K    = fzero(intb, cr);

% substitution: total profiles
aG = aG(K);
aL = 1 - aG;


% D. densities
rho  = aG * rhoG + aL * rhoL;        % rho(r)
rhoM = trapz(rho .* r)/trapz(r);     % mixture average rho


% E. law of the wall
% multiphase friction velocity
Ux = sqrt( D/4 * ( 1/rhoM * trapz(-dpdz .* r)/trapz(r) - g) );

% loop terminate condition:
% area-averaged dp/dz must be larger than mixture hydrostatic to ensure
% upward flow, ie. Ux > 0.
if  le(Ux,0)
    fprintf('ERROR \nloop terminated: <dpdz> should exceed <rho> * g');
    break
end
```

```
% log layer profile (enforce no slip bc at end)
logL      = Ux * ( 1/k * log((D/2 - r) * Ux * rhoL/muL) + 5 );
logL(end) = 0;


% F. streamwise liquid velocity Uz(r) -- core part
% non-homogeneous mixture stress profile
Trz = 1./r .* cumtrapz( dr, ( -dpdz - rho * g ) .* r );

% solve ODE for core velocity
F    = 1 ./ (L^2 * rho) .* Trz;
Uc   = cumtrapz( dr, -sign(F) .* sqrt(abs(F)) );

% profile matching to log layer @ r/D = 0.43
[m,n] = min( abs(r - 0.43*D) ); clear m;
Uc    = Uc + (logL(n) - Uc(n));

% total velocity profile
Uz = [Uc(1:n) logL((n+1):end)];


% G. redefine parameters
ig  = U0;
adu = abs(gradient(Uc,dr));
vt  = L^2 * adu + 0.6 * d * aG .* U0;    % local vt w/ Sato correlation

end


% POST-LOOP QUANTITIES:
% --------------------
jL = 1/A * ( 2 * pi * trapz(dr, aL .* Uz .* r) );
S  = 1/(A * D/2 * jL^2) * ( 2 * pi * trapz(dr, Uth .* Uz .* r.^2) );
UM = aG .* (Uz + U0) + aL .* Uz;
```

```
% VARIABLES
g = 9.81;                % gravitational acceleration (m/s2)
d = 0.0025;              % bubble diameter (m)

% geometry
D  = 0.0814;             % pipe diameter (m)
A  = pi/4 * D^2;         % cross-sectional area (m2)
dr = D/1000;             % radial step size
r  = dr:dr:D/2;

x  = r/D;                % nondimensional radial coordinate (-)

% fluid parameters
rhoL = 1000;
muL  = 1e-3;
rhoG = 1.2;
muG  = 18e-6;

% law of the wall
k = 0.4;                 % Von Kármán constant

%
dim = size(r);
```

Bibliography

[1] Wu, B., Firouzi, M., et al. (2017) *A critical review of flow maps for gas-liquid flows in vertical pipes and annuli*, Chemical Engineering Journal 326, pp. 350–377.
https://doi.org/10.1016/j.cej.2017.05.135

[2] Taitel, Y., Dukler, A.E. (1976) *A model for predicting flow regime transitions in horizontal and near horizontal gas-liquid flow*, AIChE Journal, vol. 22, no. 1, pp. 47–55.
https://doi.org/10.1002/aic.690220105

[3] Taitel, Y., Barnea, D., Dukler, A.E. (1980) *Modelling flow pattern transitions for steady upward gas-liquid flow in vertical tubes*, AIChE Journal, vol. 26, no. 3, pp. 345–354.
https://doi.org/10.1002/aic.690260304

[4] Barnea, D. (1987) *A unified model for predicting flow-patterns transitions for the whole range of pipe inclinations*, Int. J. Multiphase Flow, vol. 13, no. 1, pp. 1–12.
https://doi.org/10.1016/0301-9322(87)90002-4

[5] Mishima, K., Ishii, M. (1984) *Flow regime transition criteria for upward two-phase flow in vertical tubes*, Int. J. Heat Mass Transfer, vol. 27, no. 5, pp. 723–737.
https://doi.org/10.1016/0017-9310(84)90142-X

[6] Shakutsui, H., Hayashi, K., Suzuki, T. (2010) *Flow patterns of gas-liquid two-phase swirling flow in a vertical pipe*, Japanese J. Multiphase Flow, vol. 24 (3), pp. 305–312.
https://doi.org/10.3811/jjmf.24.305

[7] Liu, L., Bai, B. (2019) *Flow regime identification of swirling gas-liquid flow with image processing technique and neural networks*, Chem. Eng. Science 199, pp. 588–601.
https://doi.org/10.1016/j.ces.2019.01.037

[8] Liu, L., Bai, B. (2019) *A mechanistic model for the prediction of swirling annular flow pattern transition*, Chem. Eng. Science 199, pp. 405–416.
https://doi.org/10.1016/j.ces.2019.01.039

[9] Liu, L., Zhang, J., Liu, S., Wang, K., Gu, H. (2021) *Decay law and swirl length of swirling gas-liquid flow in a vertical pipe*, Int. J. Multiphase Flow, vol. 137, no. 4.
https://doi.org/10.1016/j.ijmultiphaseflow.2021.103570

[10] Lopez de Bertodano, M., Lahey, R.T., Jones, O.C. (1994) *Phase distribution in bubbly two-phase flow in vertical ducts*, Int. J. Multiphase Flow, vol. 20, no. 5, pp. 805–818.
https://doi.org/10.1016/0301-9322(94)90095-7

[11] Drew, D.A., Lahey, R.T. (1982) *Phase-distribution mechanisms in turbulent low-quality two-phase flow in a circular pipe*, J. Fluid Mech., vol. 117, pp. 91–106.
https://doi.org/10.1017/S0022112082001530

[12] Sato, Y., Sadatomi, M. (1981) *Momentum and heat transfer in two-phase bubble flow*, Int. J. Multiphase Flow, vol. 7, pp. 167–177.
https://doi.org/10.1016/0301-9322(81)90003-3

[13] Marfaing, O., Guingo, M., Laviéville, J., Bois, G., Méchitoua, N., Mérigoux, N. (2016) *An analytical relation for the void fraction distribution in a fully developed bubbly flow in a vertical pipe*, Chem. Eng. Science 152, pp. 579–585.
https://doi.org/10.1016/j.ces.2016.06.041

[14] Kataoka, H., Shinkai, Y., Tomiyama, A. (2009) *Pressure drop in two-phase swirling flow in a steam separator*, J. Power and Energy Systems, vol. 3, no. 2, pp. 382–392.
https://doi.org/10.1299/jpes.3.382

[15] Kitoh, O. (1991) *Experimental study of turbulent swirling flow in a straight pipe*, J. Fluid Mech., vol. 225, pp. 445–479.
https://doi.org/10.1017/S0022112091002124

[16] Davidson, M.R. (1990) *Numerical calculations of two-phase flow in a liquid bath with bottom gas injection*, Appl. Math. Modelling, vol. 14, no. 2, pp. 67–76.
https://doi.org/10.1016/0307-904X(90)90074-F

[17] Alekseenko, S.V., Kuibin, P.A., Okulov, V.L., Shtork, S.I. (1999) *Helical vortices in swirl flow*, J. Fluid Mech., vol. 382, pp. 195–243.
https://doi.org/10.1017/S0022112098003772

[18] Reynolds, A. (1961) *On the dynamics of turbulent vortical flow*, ZAMP J. of Applied Mathmatics and Physics, vol. 12, pp. 149–158.
https://doi.org/10.1007/BF01601014

[19] Schiller, L., Naumann, Z. (1935) *A drag coefficient correlation*,
Z. Ver. Deutsch. Ing., vol. 77, pp. 318–320.

[20] Sahovic, B., Atmani, H., Sattar, M.A., Garcia, M.M., Schleicher, E., Legendre, D., Climent, E., Zamansky, R., Pedrono, A., Babout, L., Banasiak, R., Portela, L.M., Hampel, U. (2020) *Controlled inline fluid separation based on smart process tomography sensors*, Chemie Ing. Technik, vol. 92, no. 5, pp. 554–563.
https://doi.org/10.1002/cite.201900172

[21] Frank, T., Shi, J., Burns, A.D. (2004) *Validation of eulerian multiphase flow models for nuclear safety applications*, Proc. Third Int. Symp. on two-phase modelling and experimentation, pp. 22–25.

[22] Van 't Westende, J.M.C., Kemp, H.K., Belt, R.J., Portela, L.M., Mudde, R.F., Oliemans, R.V.A. (2006) *On the role of droplets in cocurrent annular and churn-annular pipe flow*, Int. J. Multiphase Flow, vol. 33, pp. 595–615.
https://doi.org/10.1016/j.ijmultiphaseflow.2006.12.006

[23] Brennen, C.E. (2005) *Fundamentals of multiphase flow*, Cambridge University Press.
https://doi.org/10.1017/CBO9780511807169

[24] Clift, R., Grace, J.R., Weber, M.E. (1978) *Bubbles, drops and particles*,
Academic press.
ISBN 978 01 2176 950 5

[25] Mostafa Ghiasiaan, S. (2008) *Two-phase flow, boiling, and condensation*,
Cambridge University Press.
ISBN 978 05 2188 276 7

[26] Tennekes, H., Lumley, J.L. (1972) *A first course in turbulence*,
MIT Press.
ISBN 026 22 0019 8

[27] Nieuwstadt, F.T.M., Boersma, B.J., Westerweel, J. (2016) *Turbulence*, Springer International Publishing.
https://doi.org/10.1007/978-3-319-31599-7

[28] Hanjalić, K., Kenjereš, S., Tummers, M.J., Jonker, H.J.J. (2009) *Analysis and modelling of physical transport phenomena*, Delft Academic Press.
ISBN 978 90 6562 165 8

[29] Dirkzwager, M. (1996) *A new axial cyclone design for fluid-fluid separation*, PhD dissertation, TU Delft.
http://resolver.tudelft.nl/uuid:05d062a7-05d7-472a-a4f4-caba77660e76

[30] Steenbergen, W. (1995) *Turbulent pipe flow with swirl*, PhD dissertation, TU Eindhoven.
https://doi.org/10.6100/IR430720

[31] Van Campen, L.J.A.M. (2014) *Bulk dynamics of droplets in liquid-liquid axial cyclones*, PhD dissertation, TU Delft.
http://resolver.tudelft.nl/uuid:bf295221-4e6e-4663-b046-79da13325243

[32] Star, S.K. (2016) *Pressure distribution in a liquid-liquid cyclone separator*, MSc thesis, TU Delft.

[33] Karimpoorheidari, A. (2019) *A numerical study of swirl flow in pipes: application to inline swirl separators*, MSc thesis, TU Delft.
http://resolver.tudelft.nl/uuid:cb91f195-abea-4908-817d-8198fb8eadb2

[34] Ammerlaan, D. (2021) *Swirl effects on vertical gas-liquid flow regimes: Experiments and modelling*, MSc thesis, TU Delft.
http://resolver.tudelft.nl/uuid:1dede2ec-ecdd-4ea6-a42b-5204b219ead5

Support documents for experiments

[35] Garcia, M.M. (2021) *Gas-liquid inline swirl separator* (TOMOCON) *user manual*, Setup manual and safety report, TU Delft.

[36] Bronkhorst High-Tech BV (2021) *General instructions digital mass flow & pressure instruments*, document no. 9.17.022
http://www.bronkhorst.com/en-us/downloads-en/manuals-and-quick-installation-guides

[37] Endress+Hauser (2022) *Technical information: Deltabar S PMD75, FMD77, FMD78*, document no. TI00382P/00/EN/34.21
http://www.endress.com/en/field-instruments-overview/pressure/differential-pressure-deltabar

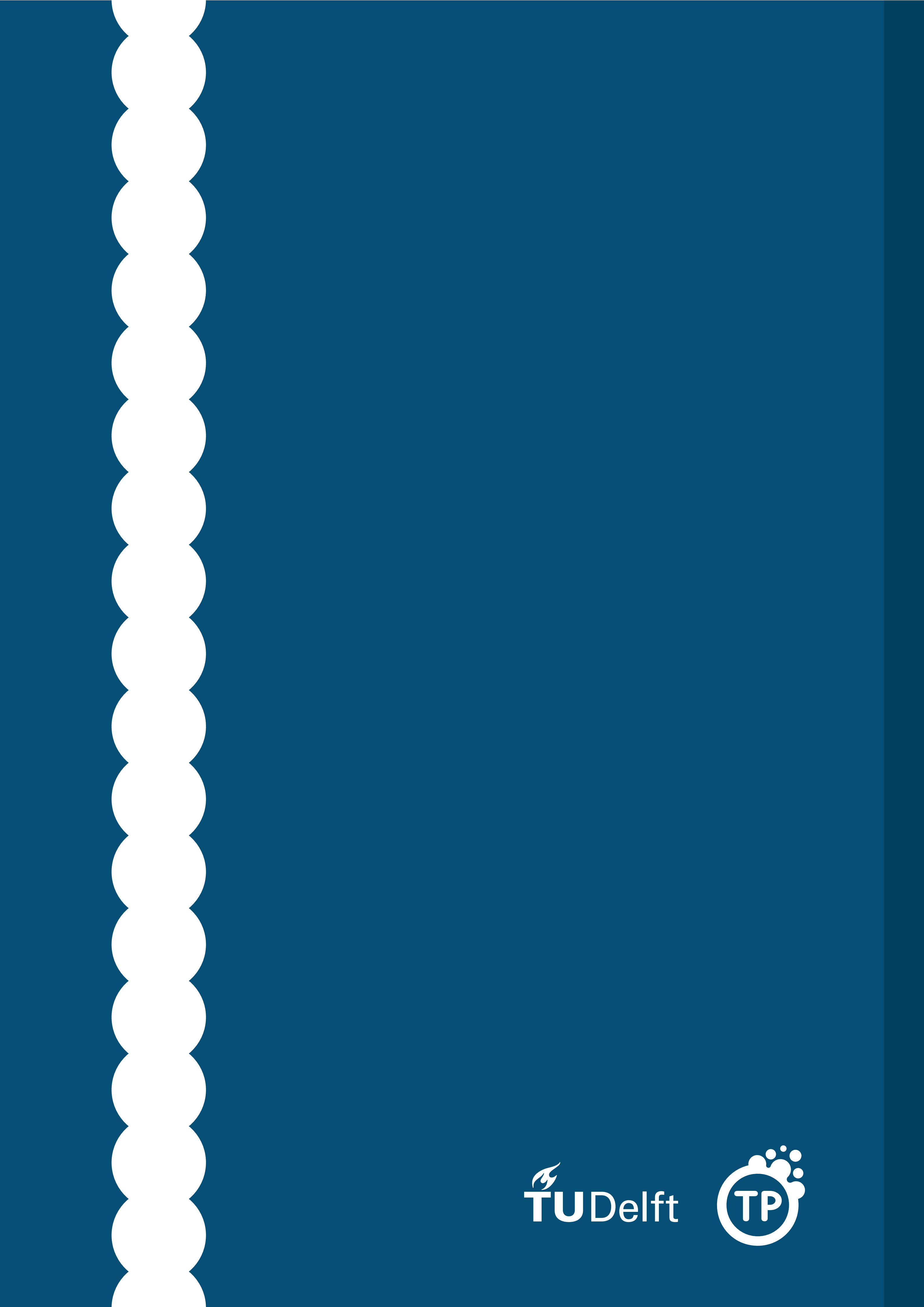
TU Delft
TP